1
Rheology of Disperse Systems

Norbert Willenbacher and Kristina Georgieva

1.1
Introduction

The rheology of disperse systems is an important processing parameter. Being able to characterize and manipulate the flow behavior of dispersions one can ensure their optimal performance. Waterborne automotive coatings, for example, should exhibit a distinct low-shear viscosity necessary to provide good leveling but to avoid sagging at the same time. Then, a strong degree of shear thinning is needed to guarantee good pump- and sprayability. The rheological properties of dispersions, especially at high solids content, are complex and strongly dependent on the applied forces and flow kinematics. Adding particles does not simply increase the viscosity of the liquid as a result of the hydrodynamic disturbance of the flow; it also can be a reason for deviation from Newtonian behavior, including shear rate dependent viscosity, elasticity, and time-dependent rheological behavior or even the occurrence of an apparent yield stress. In colloidal systems particle interactions play a crucial role. Depending on whether attractive or repulsive interactions dominate, the particles can form different structures that determine the rheological behavior of the material. In the case of attractive particle interactions loose flocs with fractal structure can be formed, immobilizing part of the continuous phase. This leads to a larger effective particle volume fraction and, correspondingly, to an increase in viscosity. Above a critical volume fraction a sample-spanning network forms, which results in a highly elastic, gel-like behavior, and an apparent yield stress. Shear-induced breakup and recovery of floc structure leads to thixotropic behavior. Electrostatic or steric repulsion between particles defines an excluded volume that is not accessible by other particles. This corresponds to an increase in effective volume fraction and accordingly to an increase in viscosity. Crystalline or gel-like states occur at particle concentrations lower than the maximum packing fraction.

Characterization of the microstructure and flow properties of dispersions is essential for understanding and controlling their rheological behavior. In this chapter we first introduce methods and techniques for standard rheological tests and then characterize the rheology of hard sphere, repulsive, and attractive particles. The effect of particle size distribution on the rheology of highly concentrated

Product Design and Engineering: Formulation of Gels and Pastes, First Edition.
Edited by Ulrich Bröckel, Willi Meier, and Gerhard Wagner.

dispersions and the shear thickening phenomenon will be discussed with respect to the influence of colloidal interactions on these phenomena. Finally, typical features of emulsion rheology will be discussed with special emphasis on the distinct differences between dispersion and emulsion rheology.

1.2
Basics of Rheology

According to its definition, rheology is the science of the deformation and flow of matter. The rheological behavior of materials can be regarded as being between two extremes: Newtonian viscous fluids, typically liquids consisting of small molecules, and Hookean elastic solids, like, for example, rubber. However, most real materials exhibit mechanical behavior with both viscous and elastic characteristics. Such materials are termed *viscoelastic*. Before considering the more complex viscoelastic behavior, let us first elucidate the flow properties of ideally viscous and ideally elastic materials.

Isaac Newton first introduced the notion of viscosity as a constant of proportionality between the force per unit area (shear stress) required to produce a steady simple shear flow and the resulting velocity gradient in the direction perpendicular to the flow direction (shear rate):

$$\sigma = \eta\dot{\gamma} \tag{1.1}$$

where $\sigma = F/A$ is the shear stress, η the viscosity, and the $\dot{\gamma} = v/h$ is the shear rate. Here A is the surface area of the sheared fluid volume on which the shear force F is acting and h is the height of the volume element over which the fluid layer velocity v varies from its minimum to its maximum value. A fluid that obeys this linear relation is called *Newtonian*, which means that its viscosity is independent of shear rate for the shear rates applied. Glycerin, water, and mineral oils are typical examples of Newtonian liquids. Newtonian behavior is also characterized by constant viscosity with respect to the time of shearing and an immediate relaxation of the shear stress after cessation of flow. Furthermore, the viscosities measured in different flow kinematics are always proportional to one another.

Materials such as dispersions, emulsions, and polymer solutions often exhibit flow properties distinctly different from Newtonian behavior and the viscosity decreases or increases with increasing shear rate, which is referred to a shear thinning and shear thickening, respectively. Figure 1.1a,b shows the general shape of the curves representing the variation of viscosity as a function of shear rate and the corresponding graphs of shear stress as a function of shear rate.

Materials with a yield stress behave as solids at rest and start to flow only when the applied external forces overcome the internal structural forces. Soft matter, such as, for example, dispersions or emulsions, does not exhibit a yield stress in this strict sense. Instead, these materials often show a drastic change of viscosity by orders of magnitude within a narrow shear stress range and this is usually termed an *"apparent" yield stress* (Figure 1.2a,b). Dispersions with attractive interactions,

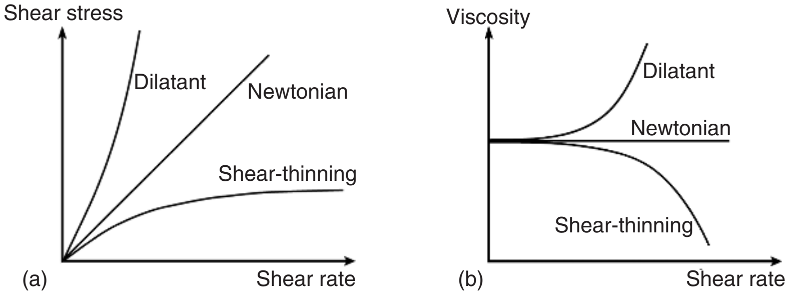

Figure 1.1 Typical flow curves for Newtonian, shear thinning and shear thickening (dilatant) fluids: (a) shear stress as a function of shear rate; (b) viscosity as a function of shear rate.

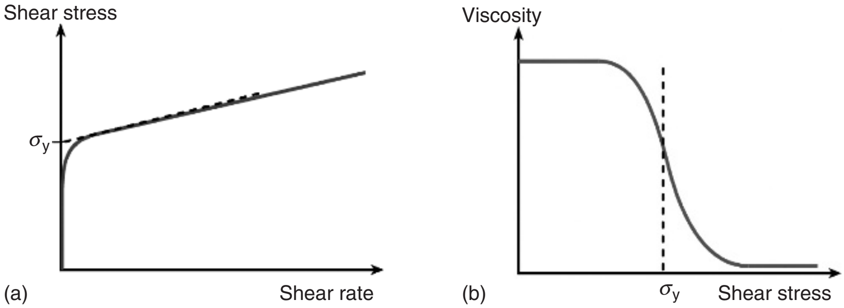

Figure 1.2 Flow curve of a material with an apparent yield stress σ_y: (a) shear stress as a function of shear rate; (b) viscosity as a function of shear stress.

such as emulsions and foams, clay suspensions, and ketchup, are typical examples of materials with an apparent yield stress. Note that there are various methods for yield stress determination and the measured value may differ depending on the method and instrument used.

The flow history of a material should also be taken into account when making predictions of the flow behavior. Two important phenomena related to the time-dependent flow behavior are thixotropy and rheopexy. For materials showing thixotropic behavior the viscosity gradually decreases with time under constant shear rate or shear stress followed by a gradual structural recovery when the stress is removed. The thixotropic behavior can be identified by measuring the shear stress as a function of increasing and decreasing shear rate. Figure 1.3 shows a hysteresis typical for a thixotropic fluid. Examples of thixotropic materials include coating formulations, ketchup, and concentrated dispersions in the two-phase region (Section 1.4.1.1). The term *rheopexy* is defined as shear-thickening followed by a gradual structural recovery when the shearing is stopped. Tadros pointed out that rheopexy should not be confused with anti-thixotropy, which is the time dependent shear thickening [1]. However, rheopectic materials are not very common and will not be discussed here.

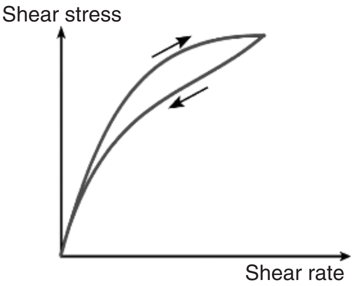

Figure 1.3 Flow curve of a thixotropic material.

So far we have considered the flow behavior of viscous fluids in terms of Newton's law and a nonlinear change of viscosity with applied stress that can occur either instantaneously or over a long period of time. At the other extreme is the ideal elastic behavior of solids, which can be described by Hooke's law of elasticity:

$$\sigma = G\gamma \tag{1.2}$$

where γ is the shear deformation (also termed *strain*) and G is the shear modulus characterizing the rigidity of a material. The shear modulus of an ideal elastic solid is independent of the shear stress and duration of the shear load. As soon as a deformation is applied a constant corresponding stress occurs instantaneously. In viscoelastic materials stress relaxes gradually over time at constant deformation and eventually vanishes for viscoelastic liquids. When the stress relaxation is proportional to the strain we are talking about the so-called linear viscoelastic regime. Above a critical strain the apparent shear modulus becomes strain dependent. This is the so-called nonlinear viscoelastic regime. The linear viscoelastic material properties are in general very sensitive to microstructural changes and interactions in complex fluids.

A dynamic test or small amplitude oscillatory shear (SAOS) test is the most widely used rheological measurement to investigate the linear viscoelastic behavior of a fluid, since it has a superior accuracy compared to step strain or step stress experiments. When a sinusoidal oscillatory shear strain is applied with amplitude γ_0 and angular frequency ω the deformation $\gamma(t)$ can be written as:

$$\gamma(t) = \gamma_0 \sin(\omega t) \tag{1.3}$$

where t denotes the time. The shear rate is the time derivative of the shear strain and then reads as follows:

$$\dot{\gamma}(t) = \frac{\mathrm{d}\gamma(t)}{\mathrm{d}t} = \gamma_0 \omega \cos(\omega t) \tag{1.4}$$

A linear viscoelastic fluid responds with a sinusoidal course of shear stress $\sigma(t)$ with amplitude σ_0 and angular frequency ω, but is phase shifted by an angle δ compared to the imposed strain:

$$\sigma(t) = \sigma_0 \sin(\omega t + \delta) \tag{1.5}$$

Depending on material behavior, the phase shift angle δ occurs between 0° and 90°. For ideal elastic materials the phase shift disappears, that is, $\delta = 0$, while for ideal viscous liquids $\delta = 90^\circ$. The shear modulus can be written in complex form:

$$G^*(\omega) = G'(\omega) + \mathrm{i}G''(\omega) \tag{1.6}$$

with the storage modulus G' and loss modulus G''. G' is a measure of the energy stored by the material during a cycle of deformation and represents the elastic behavior of the material, while G'' is a measure of the energy dissipated or lost as heat during the shear cycle and represents the viscous behavior of the material. The terms G' and G'' can be expressed as sine and cosine function of the phase shift angle δ:

$$G'(\omega) = \frac{\sigma_0}{\gamma_0} \cos\delta \tag{1.7}$$

$$G''(\omega) = \frac{\sigma_0}{\gamma_0} \sin\delta \tag{1.8}$$

Hence the tangent of the phase shift δ represents the ratio of loss and storage modulus:

$$\tan\delta = \frac{G''(\omega)}{G'(\omega)} \tag{1.9}$$

Analogous to the complex shear modulus we can define a complex viscosity η^*:

$$\eta^*(\omega) = \frac{\sigma(t)}{\dot{\gamma}(t)} = \eta'(\omega) + \mathrm{i}\eta''(\omega) \tag{1.10}$$

with:

$$\eta'(\omega) = \frac{G''(\omega)}{\omega} \quad \text{and} \quad \eta''(\omega) = \frac{G'(\omega)}{\omega} \tag{1.11}$$

The viscoelastic properties of a fluid can be characterized by oscillatory measurements, performing amplitude- and frequency-sweep. The oscillatory test of an unknown sample should begin with an amplitude sweep, that is, variation of the amplitude at constant frequency. Up to a limiting strain γ_c the structure of the tested fluid remains stable and G' as well as G'' is independent of the strain amplitude. The linear viscoelastic range may depend on the angular frequency ω; often, γ_c decreases weakly with increasing frequency.

Frequency sweeps are used to examine the time-dependent material response. For this purpose the frequency is varied using constant amplitude within the linear viscoelastic range. At an appropriately high angular frequency ω, that is, short-term behavior, the samples show an increased rigidity and hence $G' > G''$. At lower frequencies (long-term behavior) stress can relax via long-range reorganization of the microstructure and the viscous behavior dominates and, correspondingly, $G'' > G'$.

1.3
Experimental Methods of Rheology

Rheometers can be categorized according to the flow type in which material properties are investigated: simple shear and extensional flow. Shear rheometers can be divided into rotational rheometers, in which the shear is generated between fixed and moving solid surfaces, and pressure driven like the capillary rheometer, in which the shear is generated by a pressure difference along the channel through which the material flows. Extensional rheometers are far less developed than shear rheometers because of the difficulties in generating homogeneous extensional flows, especially for liquids with low viscosity. Many different experimental techniques have been developed to characterize the elongational properties of fluids and predict their processing and application behavior, including converging channel flow [2], opposed jets [3], filament stretching [4], and capillary breakup [5, 6] techniques. However, knowledge about the extensional rheology of complex fluids like dispersions and emulsions is still very limited.

1.3.1
Rotational Rheometry

Rotational instruments are used to characterize materials in steady or oscillatory shear flow. Basically there are two different modes of flow: controlled shear rate and controlled shear stress. Three types of measuring systems are commonly used in modern rotational rheometry, namely, concentric cylinder, parallel plate, and cone-and-plate. Typical shear rates that can be measured with rotational rheometers are in the range 10^{-3} to 10^{3} s^{-1}.

1.3.1.1 Concentric Cylinder Measuring System

As shown in Figure 1.4a, a cylinder measuring system consists of an outer cylinder (cup) and an inner cylinder (bob). There are two modes of operation depending on whether the cup or the bob is rotating. The Searle method corresponds to a

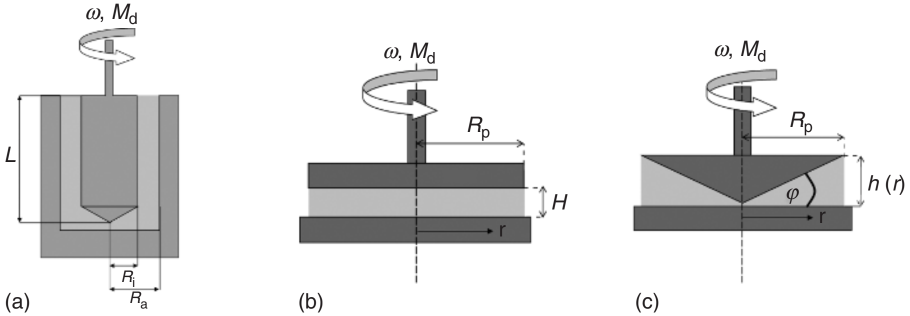

Figure 1.4 Schematic representation of (a) concentric cylinder, (b) parallel-plate, and (c) cone-and-plate measuring system.

rotating bob and stationary cup, while in the Couette mode the cup is set in motion and the bob is fixed. The gap between the two concentric cylinders should be small enough so that the sample confined in the gap experiences a constant shear rate. This requirement is fulfilled and the gap is classified as ''narrow'' when the ratio of the inner to the outer cylinder radius is greater than 0.97.

When the bob is rotating at an angular velocity ω the shear rate is given by:

$$\dot{\gamma} = 2\omega \frac{R_\mathrm{a}^2}{R_\mathrm{a}^2 - R_\mathrm{i}^2} \tag{1.12}$$

where R_i and R_a are the radii of the bob and the cup, respectively. If the torque measured on the bob is M_d, the shear stress σ in the sample is given by:

$$\sigma = \frac{M_\mathrm{d}}{2\pi R_\mathrm{i}^2 L} \tag{1.13}$$

where L is the effective immersed length of the bob.

Having the shear rate $\dot{\gamma}$ and shear stress σ, the sample viscosity η can be calculated according to Equation 1.1 For these calculations we ignore any end effects, which are actually likely to occur as a result of the different shearing conditions in the liquid covering the ends of the cylinders. To minimize the end effect the ratio of the length L to the gap between cylinders is maintained at greater than 100 and the shape of the bottom of the bob is designed as a cone with an angle α, which is chosen so that the shear rate in the bottom area matches that in the narrow gap between the concentric cylinders.

The concentric cylinder measuring system is especially suitable for low-viscous liquids, since it can be designed to offer a large shear area and at high shear rates the sample is not expelled from the gap. Other advantages of this geometry are that sample evaporation is of minor relevance since the surface area is small compared to the sample volume, the temperature can be easily controlled due to the large contact area, and even if suspensions exhibit sedimentation and particle concentration varies along the vertical direction the measured viscosity is a good approximation of the true value.

1.3.1.2 **Parallel-Plate Measuring System**

The parallel plate geometry is shown in Figure 1.4b. The sample, confined within the gap of height H between the two parallel plates, is sheared by the rotation of one of the plates at angular velocity ω. Thereby, the circumferential velocity v depends on the distance from the plate at rest h and the distance r from the rotational axis:

$$v(r,h) = r\omega \frac{h}{H} \tag{1.14}$$

and thus:

$$\dot{\gamma}(r) = \frac{v}{h} = \frac{r\omega}{H} \tag{1.15}$$

The shear rate $\dot{\gamma}$ at constant ω is not constant within the gap. Typically, the calculations and analysis of rheological results in parallel-plate measuring systems are related to the maximum shear rate value at the rim of the plate ($r = R_\mathrm{p}$). The shear rate can be varied over a wide range by changing the gap height H and the angular velocity ω.

The shear stress σ is a function of the shear rate $\dot{\gamma}$, which is not constant within the gap. Thus, to relate the shear stress to the total torque an expression for the $\sigma(\dot{\gamma})$ dependence is necessary. For Newtonian liquids the shear stress depends linearly on the shear rate and can be expressed as follows:

$$\sigma(R) = \frac{2M_\mathrm{d}}{\pi R_\mathrm{p}^3} \tag{1.16}$$

This expression is called the *apparent shear stress*. For non-Newtonian fluids Giesekus and Langer [7] developed a simple approximate single point method to correct the shear rate data, based on the idea that the true and apparent shear stress must be equal at some position near the wall. It was found that this occurs at the position where $r/R_\mathrm{p} = 0.76$ and this holds for a wide range of liquids.

The parallel-plate measuring system allows for measurements of suspensions with large particles by using large gap heights. On the other hand, by operating at small gaps the viscosity can be obtained at relatively high shear rates. Small gaps also allow for a reduction of errors due to edge effects and secondary flows. Wall slip effects can be corrected by performing measurements at different gap heights. Rough plates are often used to minimize wall slip effects. Note that for sedimenting suspensions the viscosity is systematically underestimated since the upper rotating plate moves on a fluid layer with reduced particle loading.

1.3.1.3 **Cone-and-Plate Measuring System**

A cone-and-plate geometry is shown schematically in Figure 1.4c. The sample is contained between a rotating flat cone and a stationary plate. Note that the apex of the cone is cut off to avoid friction between the rotating cone and the lower plate. The gap angle φ is usually between 0.3° and 6° and the cone radius R_p is between 10 and 30 mm. The gap h increases linearly with the distance r from the rotation axis:

$$h(r) = r\tan\varphi \tag{1.17}$$

The circumferential velocity v also increases with increasing distance r:

$$v(r) = r\omega \tag{1.18}$$

Hence the shear rate is constant within the entire gap and does not depend on the radius r:

$$\dot{\gamma} = \frac{\mathrm{d}v(r)}{\mathrm{d}h(r)} = \frac{\omega}{\tan\varphi} \approx \frac{\omega}{\varphi} \tag{1.19}$$

The shear stress is related to the torque M_d on the cone:

$$\sigma = \frac{3M_\mathrm{d}}{2\pi R_\mathrm{p}^3} \tag{1.20}$$

A great advantage of the cone-and-plate geometry is that the shear rate remains constant und thus provides homogenous shear conditions in the entire shear gap.

The limited maximum particle size of the investigated sample, difficulties with avoiding solvent evaporation, and temperature gradients in the sample as well as concentration gradients due to sedimentation are typical disadvantages of the cone-and-plate measuring system.

1.3.2
Capillary Rheometer

Figure 1.5 shows a schematic diagram of a piston driven capillary rheometer. A piston drives the sample to flow at constant flow rate from a reservoir through a straight capillary tube of length L. Generally, capillaries with circular (radius R) or rectangular (width B and height H) cross-sections are used. The measured pressure drop Δp along the capillary and the flow rate Q are used to evaluate the shear stress, shear rate, and, correspondingly, viscosity of the sample.

Pressure driven flows through a capillary have a maximum velocity at the center and maximum shear rate at the wall of the capillary, that is, the deformation is essentially inhomogeneous. Assuming Newtonian behavior and fully developed, incompressible, laminar, steady flow, the apparent wall shear stress σ_a in a circular capillary with radius R is related to the pressure drop Δp by:

$$\sigma_a = \frac{\Delta p R}{2L} \tag{1.21}$$

and the apparent or Newtonian shear rate at the wall can be calculated on the basis of measured flow rate according to:

$$\dot{\gamma}_a = \frac{4Q}{\pi R^3} \tag{1.22}$$

Therefore, we can evaluate the viscosity in terms of an apparent viscosity based on Newton's postulate (Equation 1.1).

To obtain the true shear rate in the case of non-Newtonian fluids the Weissenberg–Rabinowitch correction [8] for non-parabolic velocity profiles should

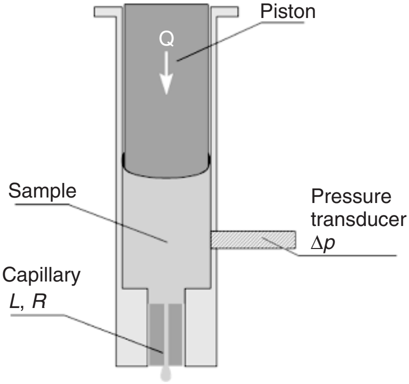

Figure 1.5 Schematic representation of a controlled flow rate capillary rheometer.

be taken into account. A simpler method to determine the true shear rate has been developed by Giesekus and Langer [7] as well as Schümmer and Worthoff [9]. Their single point method is based on the idea that the true and apparent shear rate must be equivalent at a certain radial position near the wall and thus the true shear rate $\dot{\gamma}$ is given simply by:

$$\dot{\gamma} = 0.83\dot{\gamma}_{\mathrm{a}} \tag{1.23}$$

Note that this approximation does no differ significantly from the Weissenberg–Rabinowitch correction for weakly shear thinning fluids.

Other possible sources of error in capillary flow experiments are entrance effects, slippage at the capillary wall, and viscous heating effects. Furthermore, the pressure drop Δp is difficult to measure directly in the capillary. Therefore, it is usually detected by a transducer mounted above the entrance of the capillary. Hence, the measured pressure includes not only the pressure loss due to the laminar flow in the die but also the entrance pressure loss due to rearrangement of the streamlines at the entrance and the exit of the capillary. Bagley [10] proposed a correction that accounts for these additional pressure losses but for practical purposes it is sufficient to use a single capillary die with sufficiently large L/R ratio, typically $L/R \geq 60$ [8].

For highly concentrated suspensions wall slip effects, due to shear induced particle migration (only for very large particles), and specific particle–wall interactions have to be considered. If the slip velocity is directly proportional to the applied stress it is possible to correct the apparent wall shear rate according to the procedure developed by Mooney [11], which compares the flow curves determined with dies of different radii but similar L/R.

The major advantage of the capillary rheometer is that the flow properties of fluids can be characterized under high shear conditions (up to $\dot{\gamma} = 10^6\,\mathrm{s}^{-1}$) and process-relevant temperatures (up to 400 °C). Another advantage is that the capillary flow is closed and has no free surface so that edge effects, solvent evaporation, and other problems that trouble rotational rheometry can be avoided.

1.4
Rheology of Colloidal Suspensions

The flow behavior of colloidal (often also termed *Brownian*) dispersions is controlled by the balance between hydrodynamic and thermodynamic interactions as well as Brownian particle motion. Thermodynamic interactions mainly include electrostatic and steric repulsion and van der Waals attraction. The relative importance of individual forces can be assessed on the basis of dimensionless groups, which can be used to scale rheological data. In this section we first consider dispersions of Brownian hard sphere particles and elucidate the effect of particle volume fraction, size, and shape of particles on dispersion rheology. Then, we take into account the effect of repulsive and attractive interactions on the microstructure of suspensions and its corresponding rheological response. Special attention will be paid to the rheological behavior of concentrated dispersions.

1.4.1
Hard Spheres

Hard-sphere dispersions are idealized model systems where no thermodynamic or colloidal particle–particle interactions are present unless these particles come into contact. In that sense, they represent the first step from ideal gases towards real fluids. Even such simple systems can show complex rheological behavior. The parameters controlling dispersion rheology will be discussed below.

1.4.1.1 Viscosity of Suspensions of Spheres in Newtonian Media

Hard-sphere dispersions exist in the liquid, crystalline, or glassy state depending on the particle volume fraction similar to the temperature-dependent phase transition of atomic or molecular systems. Figure 1.6 demonstrates schematically the hard-sphere phase diagram in terms of particle volume fraction ϕ, constructed by means of light diffraction measurements [12]. At a low volume fraction ϕ particles can diffuse freely and there is no long-range ordering in particle position, that is, the dispersion is in the fluid state, while with increasing concentration above $\phi = 0.50$ crystalline and liquid phases coexist in equilibrium and the fraction of crystalline phase increases until the sample is fully crystalline at $\phi = 0.55$. With further increasing particle volume fraction, crystallization becomes slower due to reduced particle mobility. At a critical volume fraction $\phi = 0.58$ particle mobility is so strongly reduced that no ordered structure can be formed and the dispersion remains in the disordered glassy (immobile) state. Crystalline ordering only occurs if all particles are of equal size, otherwise disordered gel-like structures form at $\phi > 0.5$.

The phase states of hard sphere dispersions are reflected in their characteristic flow curves. Figure 1.7 demonstrates the general features of the shear rate dependence of viscosity at various particle concentrations. At volume fractions up to $\phi = 0.50$ the dispersion is in the liquid state and a low-shear Newtonian plateau is observed for the viscosity. The low-shear viscosity, as well as the shear thinning, increases with increasing particle volume fraction ϕ. In the two-phase region colloidal hard-sphere dispersions may show thixotropic behavior (see the

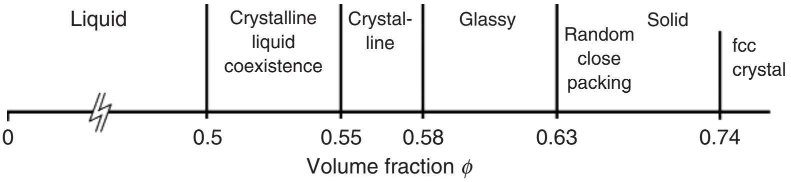

Figure 1.6 Hard-sphere phase-diagram constructed from light diffraction measurements [12].

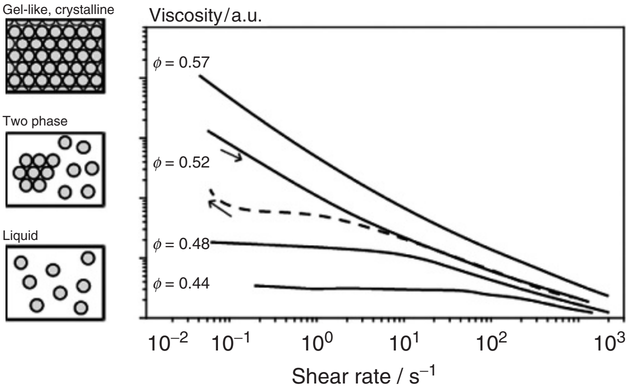

Figure 1.7 Viscosity versus shear rate for hard sphere dispersions at various volume fractions ϕ. The downward and upward arrows indicate the viscosity measurement with increasing and consequent decreasing shear rate, respectively.

curves in Figure 1.7 at $\phi = 0.52$), due to the shear induced destruction and subsequent recovery of sample structure, associated with coexisting liquid and crystalline domains. The degree of thixotropy, if any, depends on the measuring conditions. For a particle volume fraction of $\phi \geq 0.55$ dispersions are in the crystalline or gel-like state and show shear thinning behavior in the whole shear rate range investigated. On the other hand, thixotropy vanishes since no long-range particle rearrangements are possible due to the dense particle packing.

Viscosity in the low shear Newtonian plateau, referred to as *zero-shear viscosity* η_0, depends only on the total volume occupied by the particles and is independent of particle size. The solvent viscosity η_s always acts as a constant pre-factor, and in the following we will focus on the relative viscosity $\eta_r = \eta/\eta_s$. Various models describing the volume fraction dependence of the zero-shear viscosity have been proposed. The classical model of Einstein [13, 14] for infinitely dilute, non-interacting hard spheres showed that single particles increase the viscosity of the dispersion medium as a linear function of the volume fraction ϕ according to the equation:

$$\eta_r = (1 + 2.5\phi) \tag{1.24}$$

The Einstein equation applies to $\phi < 0.01$, assuring that the flow around a particle does not influence the velocity field of any other particle. At higher particle concentration the hydrodynamic interactions between particles become important and higher-order terms in ϕ have to be considered. The effect of two-sphere hydrodynamic interactions on the suspension viscosity was calculated by Batchelor [15]:

$$\eta_r = 1 + 2.5\phi + 6.2\phi^2 \tag{1.25}$$

This equation is validated to $\phi < 0.1$. For higher particle concentrations multi-particle interactions become imperative and a prediction of viscosity from first principles is still lacking. Numerous phenomenological equations have been introduced to correlate the viscosity of concentrated dispersions to the particle volume fraction. Krieger and Dougherty [16] proposed a semi-empirical equation for the concentration dependence of the viscosity:

$$\eta_r = \left(1 - \frac{\phi}{\phi_{max}}\right)^{-2.5\phi_{max}} \tag{1.26}$$

where ϕ_{max} is the maximum packing fraction or the volume fraction at which the zero shear viscosity diverges. This equation reduces to the Einstein relation (Equation 1.24) at low particle concentration. Quemada [17] suggested another phenomenological model to predict the $\eta_r(\phi)$ dependence:

$$\eta_r = \left(1 - \frac{\phi}{\phi_{max}}\right)^{-2} \tag{1.27}$$

This model suits best as $\phi \to \phi_{max}$. Figure 1.8 shows the volume fraction dependence of relative viscosity, according to the models described above.

The absolute value for the maximum packing fraction ϕ_{max} is determined by the packing geometry, which depends on the particle shape and particle size distribution but not on particle size. The volume fraction at maximum packing has been calculated by theoretical models and different ϕ_{max} values have been found depending on the type of packing. The ϕ_{max} value for hard spheres is often taken as 0.64 [18], which is the value associated with random close packing. However, experiments on colloidal hard sphere dispersions have shown that zero-shear viscosity diverges at the volume fraction of the colloidal glass transition $\phi_g = 0.58$ [19–22]. Above ϕ_g, particle diffusion is restricted to small "cages" formed

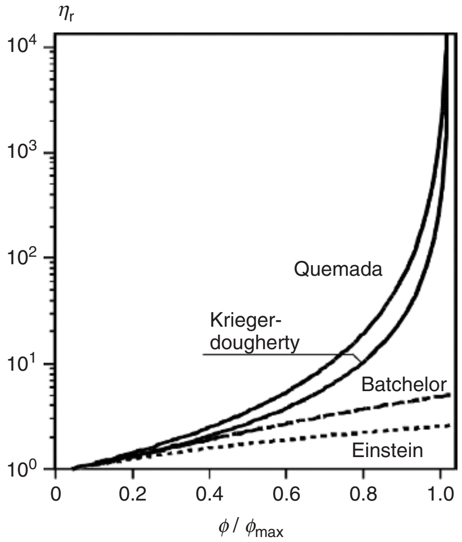

Figure 1.8 Schematic representation of the volume fraction dependence of relative viscosity η_r according to the Einstein, Batchelor, Krieger–Dougherty, and Quemada models.

by the nearest neighbors; correspondingly, the long-time self-diffusion coefficient decreases to zero and the viscosity diverges. The latter two quantities are related to each other by the generalized Stokes–Einstein equation:

$$D = \frac{k_B T}{6\pi\eta(\phi)a} \tag{1.28}$$

Let us now consider the shear rate dependence of dispersion viscosity in the liquid state. The transition from low shear to high shear plateau referred to as the *shear-thinning region* depends on the balance between Brownian and hydrodynamic forces. The Péclet number Pe is a useful dimensionless quantity to express the relative importance of these two contributions:

$$\mathrm{Pe} = \frac{6\pi a^3\eta}{k_B T}\dot{\gamma} = \frac{a^2}{D_0}\dot{\gamma} \tag{1.29}$$

where a is the particle size, $k_B T$ is the thermal energy, and $D_0 = D\ (\phi \rightarrow 0)$ is the diffusion coefficient.

The Péclet number is often called the *dimensionless shear rate*; equivalently, the dimensionless shear stress σ_r can be expressed as follows:

$$\sigma_r = \frac{a^3\sigma}{k_B T} \tag{1.30}$$

The shear thinning region occurs around a characteristic Péclet number $\mathrm{Pe} \approx 1$ at which Brownian and hydrodynamic forces are of similar relevance, which strongly depends on the particle size a. A variation of particle size results in a shift of the viscosity/shear rate curve on the $\dot{\gamma}$-axis with a shift factor proportional to the particle radius cubed. Hence a plot of η_r as a function of Péclet number or the dimensionless shear stress σ_r should superimpose for hard sphere colloids of different particle size at a given ϕ. This is illustrated in Figure 1.9a,b using the example of poly(methyl methacrylate) spheres of different size, dispersed in silicone oil , $\eta_{0,r}$ and $\eta_{\infty,r}$ denote the low and high shear limiting values of the relative viscosity.[23].

Figure 1.10a demonstrates schematically the effect of solvent viscosity η_s on the viscosity of hard-sphere dispersions. The Pe number fully accounts for the effect of viscosity of dispersion medium on the shear rate dependence of viscosity and can be used to scale the data onto a master curve (Figure 1.10b) if again the relative viscosity $\eta_r = \eta/\eta_s$.

1.4.1.2 **Non-spherical Particles**

Particles can deviate from the spherical form by either being axisymmetric or by having an irregular shape. Typically, particles are approximated by prolate or oblate spheroids (Figure 1.11) with a specified axis ratio r_p:

$$r_p = \frac{a}{b} \tag{1.31}$$

where a corresponds to the length of the semi-major axis and b to the length of the semi-minor axis. Some examples of spheroids are shown in Figure 1.11.

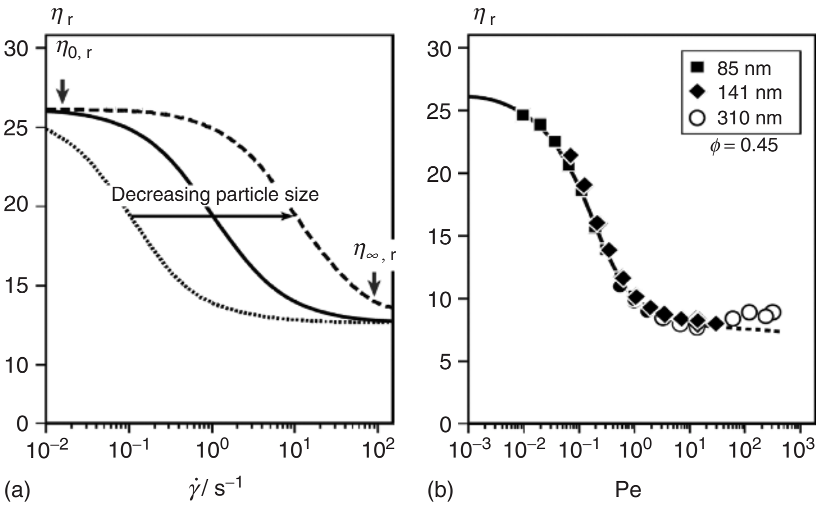

Figure 1.9 Effect of particle size on the shear rate dependence of relative viscosity. (a) Schematic representation of the flow curves of hard sphere dispersion, shifted to high shear rates as the particle size decreases; (b) relative viscosity η_r as a function of Péclet number Pe for sterically stabilized poly(methyl methacrylate) particles of different size. Redrawn from Choi and Krieger [23].

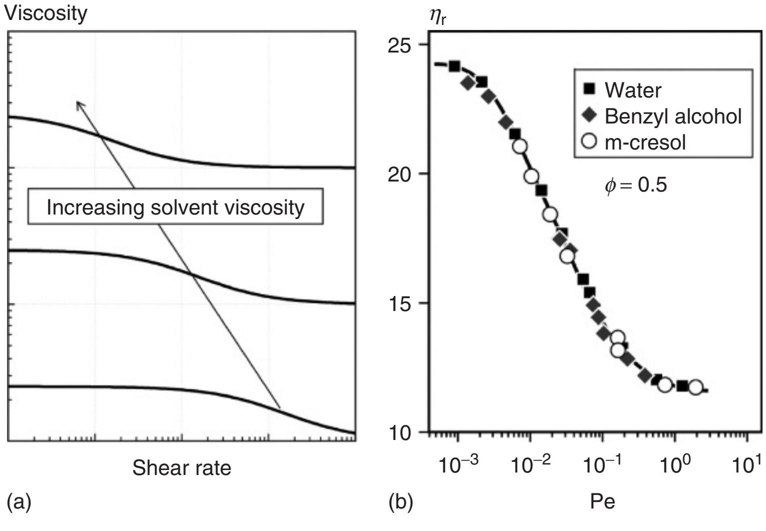

Figure 1.10 Effect of solvent viscosity on the shear rate dependence of relative viscosity. (a) Schematic representation of the flow curves for hard spheres dispersed in solvents with different viscosity; (b) relative viscosity η_r versus Pe number for polystyrene monodispersed spheres in different media. Redrawn from the paper by Krieger [24].

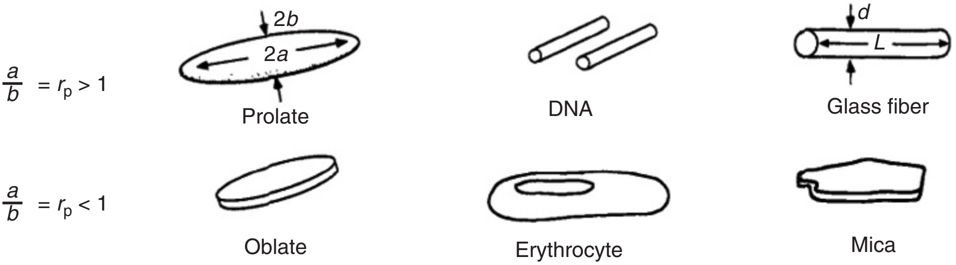

Figure 1.11 Prolate or oblate shaped particles and corresponding examples of typical particles. Taken from Macosko [8]. Copyright © 1994 John Wiley & Sons.

The rheology of suspensions of non-spherical particles is greatly influenced by particle orientation with respect to the flow. The orientation in flowing suspensions is governed by the balance between hydrodynamic forces, which tend to align particles with flow, and Brownian motion randomizing the orientation. The relative importance of each is given by a rotational Péclet number $\mathrm{Pe_{rot}}$:

$$\mathrm{Pe_{rot}} = \tau_{\mathrm{rot}}\dot{\gamma} \tag{1.32}$$

For disk-like particles with radius b, the rotational relaxation time τ_{rot} is:

$$\tau_{\mathrm{rot}}^{-1} = \frac{3k_{\mathrm{B}}T}{32\eta_{\mathrm{s}}b^3} \tag{1.33}$$

and for rod-like particles with length $2a$ such that $r_{\mathrm{p}} \gg 1$:

$$\tau_{\mathrm{rot}}^{-1} = \frac{3k_{\mathrm{B}}T(\ln 2r_{\mathrm{p}} - 0.5)}{8\pi\eta_{\mathrm{s}}a^3} \tag{1.34}$$

At low shear rates for small particles and low fluid viscosity $\mathrm{Pe_{rot}} \to 0$ and the randomizing effect of Brownian motion dominates. For $\mathrm{Pe_{rot}} > 1$ the hydrodynamic forces become enough strong to align the particles with the flow and the suspension shows a considerable shear thinning behavior.

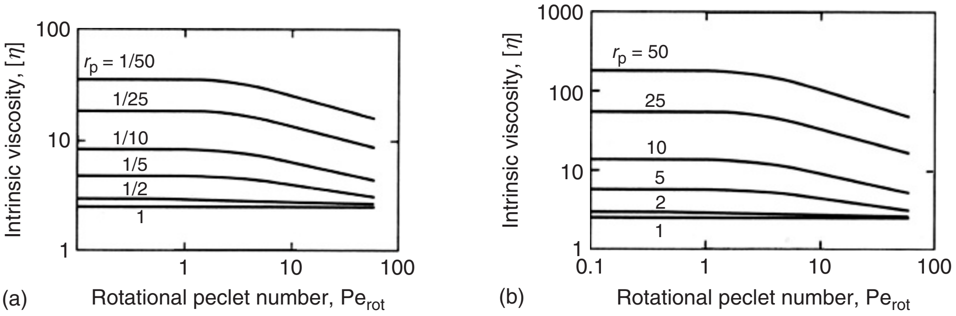

Figure 1.12 Intrinsic viscosity $[\eta]$ as a function of rotational Péclet number $\mathrm{Pe_{rot}}$, calculated for diluted suspensions of (a) disc- and (b) rod-like particles of various aspect ratios [25].

Figure 1.12a,b shows numerical results for the intrinsic viscosity $[\eta]$ as a function of $\mathrm{Pe}_{\mathrm{rot}}$ for dilute suspensions of disk- and rod-like particles at different aspect ratios [25]. The intrinsic viscosity $[\eta]$ is a dimensionless quantity defined as:

$$[\eta] = \lim_{\phi \to 0} \frac{\eta - \eta_s}{\phi \eta_s} \tag{1.35}$$

It can be seen from Figure 1.12a,b that the zero-shear intrinsic viscosity increases with increasing aspect ratio r_p, which is due to the effective enlargement of the volume inaccessible for other particles. Elongated particles in highly diluted suspensions can rotate freely about their center of gravity and thus occupy a spherical volume with a diameter corresponding to the long dimension of the spheroid. Therefore, particle interactions become relevant beyond a critical volume fraction $\phi^* \ll \phi_{\max}$ at which these spheres start to interpenetrate. Hence, particle asymmetry has a strong effect on the concentration dependence of relative viscosity.

In colloidal as well as non-colloidal suspensions axisymmetric particles could be packed more densely than spheres, but the divergence of the zero shear viscosity occurs at lower volume fraction, which decreases with increasing aspect ratio r_p (Figure 1.13).

For anisotropic particles random orientation leads to a higher barrier against flow at low shear rates, that is, to an increase in zero-shear viscosity. However,

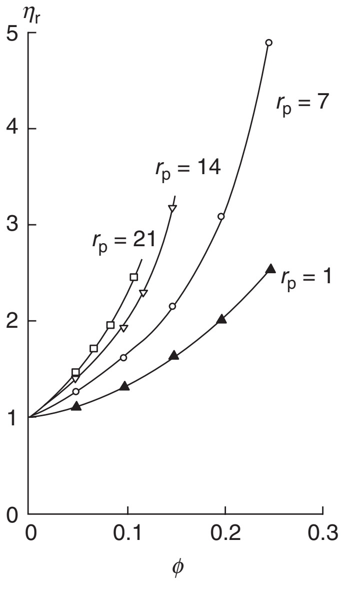

Figure 1.13 Relative viscosity η_r versus particle volume fraction ϕ for non-colloidal glass fiber suspension of various aspect ratios r_p [26]. Taken from Barnes *et al.* [27].

under shear, these elongated particles can orient in the direction of flow, resulting in a lower high shear viscosity than for spherical particles with equivalent size.

1.4.2
Influence of Colloidal Interactions on Rheology

1.4.2.1 Repulsive Particles

So far we have considered suspensions of hard spheres for which the colloidal or thermodynamic interactions did not play a role. In practice, dispersions are stabilized by repulsive surface forces in order to prevent aggregation. Colloidal interactions such as electrostatic or steric repulsion keep particles far enough apart so that they cannot be attracted by the short-range van der Waals attraction force. This corresponds to an excluded volume that is inaccessible to other particles. The effective volume fraction of the dispersion ϕ_{eff} can be expressed as follows:

$$\phi_{\text{eff}} = \phi\left(\frac{a_{\text{eff}}}{a}\right)^3 \tag{1.36}$$

where a_{eff} is the *effective particle radius* defined as half the distance to which two particle centers can approach each other under the action of colloidal forces. Many rheological features are analogous to those of hard sphere dispersions and can be quantitatively described by mapping the real system onto a hard sphere system with $\phi = \phi_{\text{eff}}$. The effective increase of the volume occupied by the particles causes an increase in the zero-shear viscosity as well as a shift of the liquid to crystalline phase transition and the colloidal glass transition to lower volume fractions ϕ. Note that hard sphere mapping is only valid if the range of repulsive interactions is small compared to the particle radius, which is true for typical commercially or technically relevant dispersions, especially at high particle loading.

Derjaguin–Landau–Verwey–Overbeek (*DLVO*) theory provides a good description of the interactions among electrostatically stabilized colloidal particles (see Chapter 2 in Volume 1 [28]). The strength of the repulsion is given by the surface charge or surface potential and the range of interaction by the so-called Debye length κ^{-1}, which is inversely proportional to the square-root of the ion concentration in the liquid phase. Since the effective volume fraction ϕ_{eff} increases with increasing κ^{-1}, the viscosity of charge-stabilized dispersions depends strongly on the ionic strength of the dispersion medium and diverges at lower volume fraction than predicted for hard spheres. The concentration dependence of the zero-shear viscosity for monodispersed charged polystyrene (PS) latices of different ionic strength and particle size is shown in Figure 1.14a,b [29]. The data on the left-hand side show that the relative zero-shear viscosity $\eta_{0,\text{r}} = \eta_0/\eta_\text{s}$ diverges at a volume fraction $\phi_{\text{max,exp}}$ well below that for hard spheres and this experimental maximum volume fraction $\phi_{\text{max,exp}}$ decreases with decreasing ionic strength of the system.

Particle size is also an important parameter that influences ϕ_{eff}. Decreasing the particle radius a, at a constant volume fraction ϕ and constant ionic strength, corresponds to an increase of ϕ_{eff} and, thus, for smaller particles the zero-shear viscosity diverges at a lower particle volume fraction $\phi_{\text{max,exp}}$ [29], when keeping all other conditions the same. The hard sphere mapping concept fully accounts for

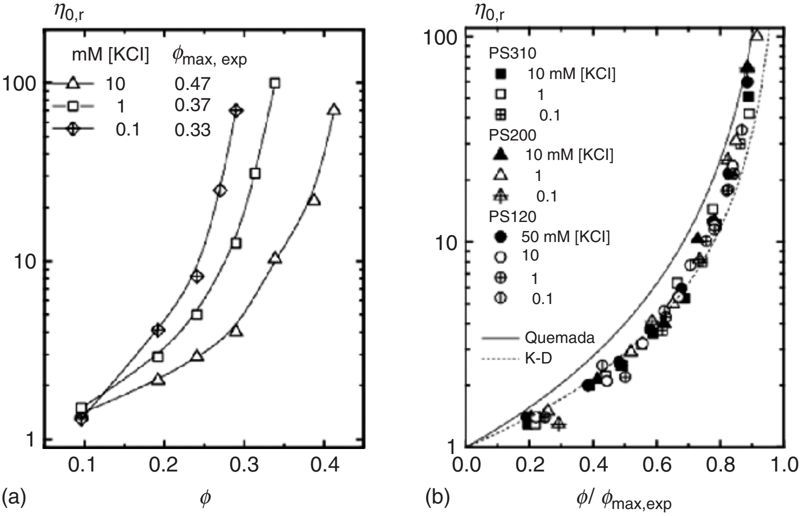

Figure 1.14 (a) Relative zero-shear viscosity $\eta_{0,r}$ versus particle volume fraction ϕ for monodisperse polystyrene particles (PS200), 200 nm in diameter, dispersed in water with concentrations of potassium chloride [KCl]; (b) master curve for all the data including the polystyrene dispersions at different salt concentration and particle size: 120, 200, and 310 nm [29].

the effects of particle size and ionic strength on the volume fraction dependence of viscosity. The zero-shear viscosity data can be collapsed onto a universal master curve by rescaling the volume fraction by $\phi/\phi_{\text{max,exp}}$ (Figure 1.14b). Furthermore, the Quemada (Equation 1.27) and Krieger–Dougherty (Equation 1.26) equations developed for hard sphere dispersions provide a good description of the zero-shear viscosity data for electrostatically interacting systems if ϕ is replaced by ϕ_{eff}.

Electrostatic interactions have a strong impact on the phase behavior of colloidal dispersions and hence on their flow properties. The hard sphere mapping concept can also be applied to categorize different characteristic signatures of the flow curves corresponding to different phase states. Figure 1.15 demonstrates the viscosity as a function of shear rate for an electrostatically stabilized PS/acrylate dispersion at various particle concentrations. Here the phase states typical for hard sphere dispersions (schematically shown in Figure 1.7) can be recognized but shifted to lower particle volume fractions. For repulsively interacting systems the phase diagram may be mapped onto that of a hard-sphere system using the effective radius concept. Accordingly, the transition volume fractions are lower than that for hard-sphere dispersion. In the example presented here, for instance, $\phi = 0.44 = \phi_{\text{lc,exp}}$ corresponds to the liquid/crystalline phase transition occurring at $\phi = 0.50 = \phi_{\text{lc,HS}}$ for hard spheres. Thus all volume fractions in this case can be rescaled as ϕ_{eff}:

$$\phi_{\text{eff}} = \phi \left(\frac{\phi_{\text{lc,HS}}}{\phi_{\text{lc,exp}}} \right) \tag{1.37}$$

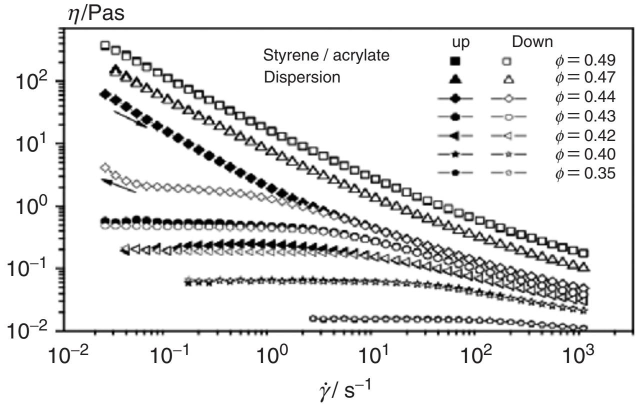

Figure 1.15 Viscosity as a function of increasing (up) and decreasing (down) shear rate for a polystyrene/acrylate dispersion ($a = 35$ nm) measured at various particle volume fractions. The downward arrow indicates the viscosity measurement with increasing the shear rate and the upward arrow indicates the subsequent measurement at gradually decreasing shear rates.

The liquid/crystalline phase transition volume fraction ϕ_{lc} decreases as the range of repulsive interaction increases.

The particle size can also influence the phase behavior of colloidal dispersions. Increasing the particle radius a at constant ϕ and a constant range of the repulsive colloidal interactions corresponds to a decreasing ϕ_{eff}. Thus, dispersions with the same ϕ but different a may exist in different phases. This has a strong impact on

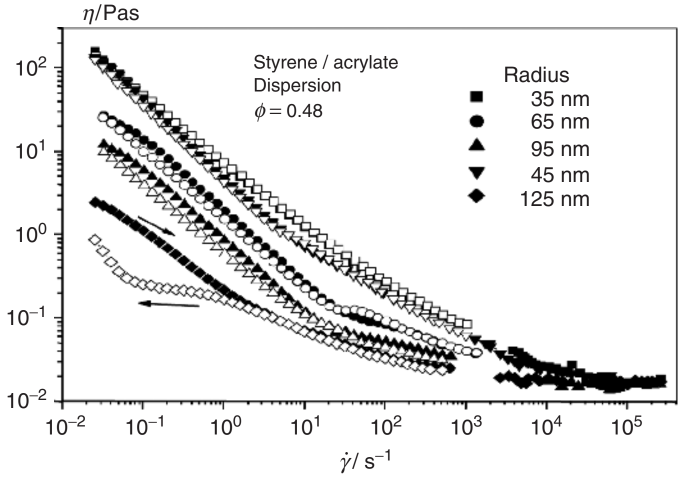

Figure 1.16 Viscosity as a function of increasing (filled symbols) and decreasing (open symbols) shear rate for polystyrene/acrylate dispersions with different particle radii measured at fixed particle volume fraction.

the shear rate dependent viscosity. Figure 1.16 demonstrates the phase transition from the crystalline to the two-phase region upon an increase of particle size of an electrostatically stabilized PS/acrylate dispersion at fixed volume fraction $\phi = 0.48$. At sufficiently high shear rates hydrodynamic interactions become dominant and can overcome the electrostatic repulsive forces so that particles approach each other closer and a_{eff} decreases until the electrostatic contribution is completely suppressed and the particles behave as hard spheres. As a consequence, the viscosity becomes independent of particle size and the flow curves superimpose.

Charged stabilized dispersions show a strong shear thinning behavior until the viscosity is close to that expected for hard spheres, that is, independent of particle size and ionic strength. This is true for the high shear viscosity η_∞ as well as the high frequency viscosity η'_∞. Note that these quantities correspond to different microstructures and η_∞ is always larger than η'_∞. The Cox–Merz rule $\eta(\dot{\gamma}) = |\eta^*(\omega)|$ for $\dot{\gamma} = \omega$, which is widely applicable for polymer melts and solutions, can be applied to dispersion rheology only at low ω and/or ϕ.

Figure 1.17 shows the frequency dependence of the elastic modulus G' and viscous modulus G'' for electrostatically stabilized suspensions at three different particle volume fractions. At low volume fraction in the liquid state $G'' \approx \omega$ dominates over $G' \approx \omega^2$, as expected for viscoelastic liquids. In the two-phase region G' and G'' are essentially equal and increase weakly according to $G^* \approx \omega^\alpha$ (power law exponent $\alpha < 1$). In the highly concentrated gel-like or crystalline state $G' \gg G''$ and both moduli are more or less independent of frequency ω.

Let us now consider the rheology of sterically stabilized dispersions. Particle repulsion in sterically stabilized dispersions results from the interactions between polymer chains or surfactant molecules adsorbed or grafted onto the particle surface. The formation of a hairy surface layer gives rise to an increase in the

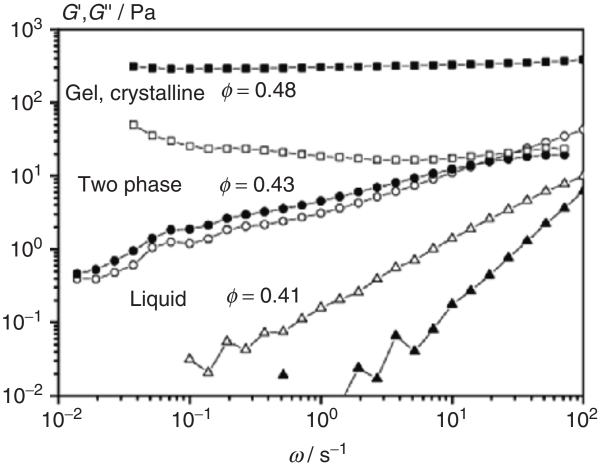

Figure 1.17 G' and G'' as a function of angular frequency ω for a concentrated electrostatically stabilized dispersion at volume fractions around the phase transition region. The filled symbols denote G', open symbols G''.

hydrodynamic particle radius and a dispersions zero-shear viscosity, in a similar way to the case of charged particles. Hence, the rheological behavior of such systems is similar to that of hard spheres with $a_{\mathrm{eff}} \approx a + L$. In particular, if the particle radius a is small the stabilizing layer can contribute significantly to the effective volume $\phi_{\mathrm{eff}} = \phi(1 + L/a)^3$; and thus give rise to a strong viscosity increase. When using polyelectrolytes or ionic stabilizers with weak functional acid groups, the thickness of the stabilizer layer L depends on the ionic strength and pH of the dispersion medium, which determine the degree of dissociation and range of electrostatic interactions among the functional acid groups. The steric repulsion provided by this surface layer, which is activated and tuned by short-range electrostatic interactions, is called *electrosteric stabilization* and is an important mechanism for stabilization of commercial polymer dispersions. As was the case for charged particles, electrosterically stabilized dispersions show universal scaling independent of ionic strength, pH, or core particle size, but here the data have to be rescaled versus ϕ_{eff} not only for the zero-shear viscosity η_0 but also for the high shear viscosity η_∞ and high frequency viscosity η'_∞. However, the hairy particles show the same η'_∞ as predicted for hard sphere dispersions up to $\phi_{\mathrm{eff}} = 0.5$. Beyond this effective volume fraction strong deviations are observed due to the permeability and interpenetration of the stabilizing layers [30].

1.4.2.2 **Attractive Particles**

Attractive particle interactions either result in large compact aggregates, which rapidly phase separate, or in loose aggregates with fractal structure. Only the latter case is relevant from a rheological point of view. Loose aggregates immobilize water, leading to a larger effective volume fraction ϕ_{eff} and thus to an increase in the zero-shear viscosity. When the shear rate is increased the flocs gradually breakdown and/or align in the flow direction, resulting in a viscosity reduction. Aggregate break-up in dilute dispersions can be estimated by the balance between hydrodynamic forces $F_{\mathrm{H}} = 6\pi\eta_{\mathrm{s}}a^2\dot{\gamma}$ and the van der Waals force $F_{\mathrm{vdW}} = aA_{\mathrm{H}}/12h^2$ (where A_{H} is the Hamaker constant and h interparticle separation distance). Hence, in the colloidal domain ($a < 1\,\mu\mathrm{m}$) very large shear rates are required to break-up the aggregates into primary particles.

The fractal structure of aggregates is characterized by the fractal dimension D_{f}, which characterizes the mass density of the flocs and is controlled by the aggregation mechanism. The lower the D_{f} value, the more open the aggregate structure is. Reaction limited- and flow-induced aggregation lead to denser structures, while diffusion limited aggregation results in low D_{f} values, as confirmed by computer simulation and scattering experiments [31–33]. Above a critical volume fraction fractal aggregates can interconnect, forming a sample-spanning network, which results in a highly elastic gel-like behavior ($G' > G''$) and an apparent yield stress. The rest structure ruptures at a critical stress level and viscosity progressively decreases with increasing applied stress. The shear induced breakdown and recovery of flocs may require a finite amount of time, resulting in thixotropic behavior.

Different flocculation mechanisms in disperse systems can be recognized:

- *Flocculation of charged particles* can be caused by increasing the ionic strength and or lowering the surface charge. Particles can then aggregate in the primary or the secondary minimum of the potential energy. The latter gives rise to fairly weak aggregates and a shear force can easily separate the particles again.
- *Flocculation of sterically stabilized particles* depends on the thickness of the stabilizing layer. Particles aggregate, when the stabilizing layer is not thick enough to screen the van der Waals attraction; as a rule of thumb, the thickness of the stabilizing layer should be $L \approx a/10$. This layer thickness strongly depends on the solvent quality of the continuous phase, and may often be widely tuned by variation of temperature. Systems with an upper or lower critical solution temperature are described in the literature.
- *Depletion flocculation* results from the osmotic pressure induced by the addition of non-adsorbing polymers. Attractive interactions in this case are easily tunable by size and concentration of added polymer.
- *Bridging flocculation* occurs on dissolving high-molecular weight polymers with a strong affinity to particle surface that attach to at least two particles. Strong bridging-flocculated gels may be formed at high particle volume fraction when the particle surface separation is small. Typically, the molecular weight of the polymers is on the order of 10^6 g mol^{-1} so that they can bridge the gap between particles without losing too much conformational entropy.
- *Flocculation by capillary forces*: the addition of small amounts of a secondary fluid, immiscible with the continuous phase of the suspension, causes agglomeration due to the capillary bridges and creates particle networks even at low particle volume fraction.

Investigations of the rheology of strongly flocculated gels are difficult because of the poor reproducibility of sample preparation, sensitivity to shear history, and preparation conditions. On the other hand, weak or reversible flocculation allows for breakup and re-formation of aggregates due to thermal forces and the structure may reach a metastable thermodynamic state.

Rheology of Weakly Flocculated Gels Suspensions in which particles are reversibly captured in a shallow primary or secondary minimum [typically $(-\Psi_{\mathrm{min}}/k_{\mathrm{B}}T) < 20$, where Ψ_{min} is the minimum of interaction potential] are classified as weakly flocculated gels. To demonstrate some features of the rheology of these weakly flocculated gels let us consider the results of the investigations of depletion flocculated suspensions and the thermoreversible gelation of sterically interacting particle suspensions. Figure 1.18a shows the shear rate dependence of the relative viscosity of colloidal dispersions of octadecyl grafted silica spheres in benzene ($\phi = 0.367$) at several temperatures [34]. When the temperature is decreased below the theta temperature (316 K) weak aggregates are formed, leading to an increase in viscosity and shear thinning behavior. Buscall *et al.* [35] studied sterically stabilized acrylic copolymer particles dispersed in "white spirit" (mixture of high-boiling hydrocarbons). Adding non-adsorbing polyisobutylene above the critical free polymer concentration for depletion flocculation causes a dramatic increase in viscosity with increasing polymer concentration (Figure 1.18b).

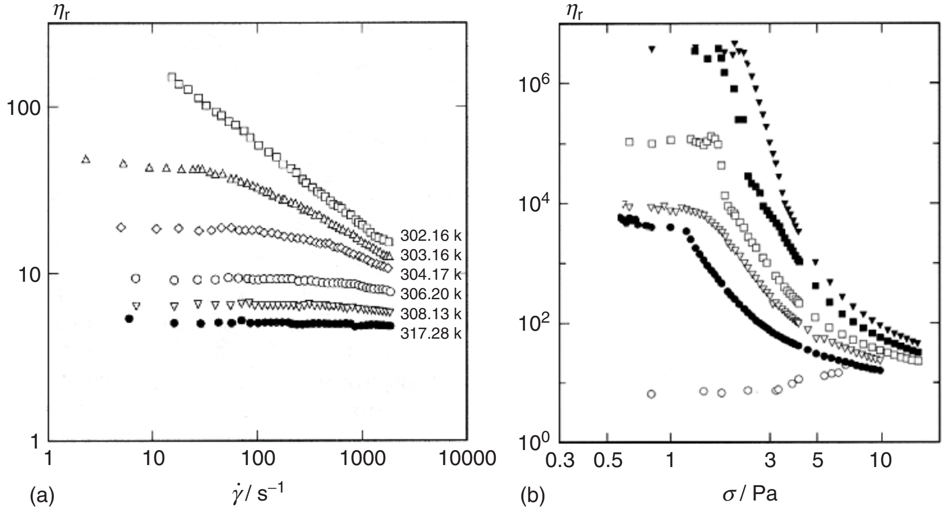

Figure 1.18 (a) Relative shear viscosity versus shear rate for a dispersion of octadecyl grafted silica spheres in benzene ($\phi = 0.367$) at several temperatures [34]; (b) relative viscosity versus shear stress σ for a dispersion of acrylic copolymer particles ($a = 157$ nm) grafted with hydroxystearic acid–poly(methyl methacrylate) and dispersed in "white spirit" at volume fraction $\phi = 0.4$ with added polyisobutene ($M_w = 411\ 000$ g mol^{-1}) of different concentrations in weight per volume: 0.1, 0.4, 0.5, 0.6, 0.85, and 1% (from bottom to top) [35].

Weakly flocculated systems are also characterized by an apparent yield stress. Tadros [1] investigated depletion flocculated aqueous PS dispersions containing free poly(ethylene oxide) (PEO) chains. It was found that the yield stress σ_y increases linearly with increasing PEO concentration ϕ_p and the slope of this linear dependence increases with increasing particle volume fraction ϕ (Figure 1.19). The following scaling relation applies:

$$\sigma_y \sim \phi^p \tag{1.38}$$

where the power-law exponent p depends on the fractal dimension and is around 3 according to experimental investigations, while numerical simulations report higher values: 3.5–4.4, depending on whether the aggregation is slow or rapid.

Figure 1.20 shows the elastic modulus G' of the depletion-flocculated aqueous PS dispersions as a function of the free polymer (PEO) volume fraction ϕ_p at several particle volume fractions. Above the critical free polymer concentration G' increases with increasing ϕ_p since the aggregates grow; G' then reaches a plateau value as soon as a sample-spanning network is formed. Furthermore, it can be seen that at any given ϕ_p the elastic modulus G' increases with increasing particle volume fraction.

Rheology of Strongly Flocculated Gels Suspensions in which particles are captured in a deep primary or secondary minimum with $(-\Psi_{\min}/k_B T) > 20$ are classified as

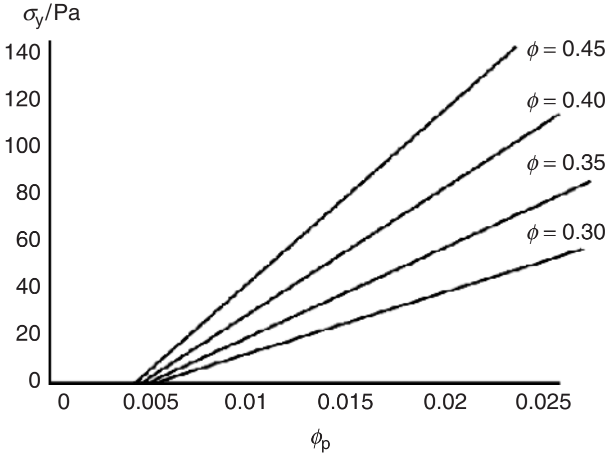

Figure 1.19 Yield stress σ_y versus free polymer (PEO, $M_w = 20\,000\,\text{g mol}^{-1}$) volume fraction ϕ_p for a polystyrene dispersion at several particle volume fractions ϕ [1].

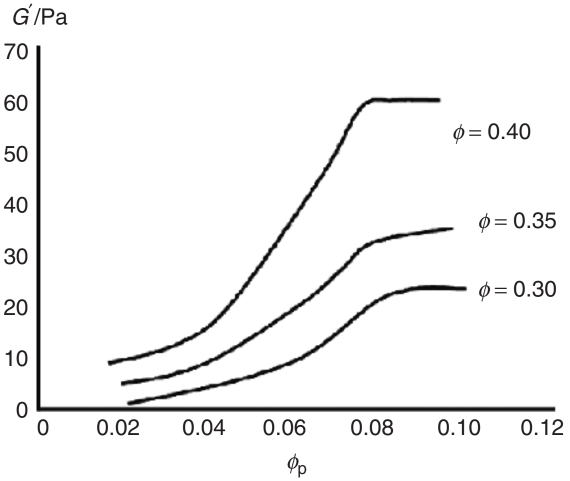

Figure 1.20 Elastic modulus G' versus free polymer (PEO, $M_w = 20\,000\,\text{g mol}^{-1}$) volume fraction ϕ_p for polystyrene dispersion ($a = 77.5$ nm) at three different particle volume fraction ϕ [1].

strongly flocculated gels. Such systems are not at equilibrium and hence difficult to investigate experimentally. Nevertheless, several studies [36–38] examined the rheological properties of strongly flocculated gels and found some typical trends for these materials. Strongly flocculated gels are highly elastic ($G' \gg G''$) at small amplitudes and have an extremely limited range of viscoelastic response. Above a critical amplitude γ_c the elastic modulus G' rapidly decreases since the flocculated structure breaks down. For strongly flocculated systems γ_c is much lower than for stable dispersions with repulsive interactions or for polymer melts and solutions. The frequency independent elastic modulus G' of strongly flocculated gels is found to be independent of particle size but strongly increases with particle volume fraction ϕ according to the following scaling law:

$$G' \sim \phi^{\alpha} \tag{1.39}$$

where the exponent α varies between 2 and 6 depending on the aggregation conditions. If aggregation is slow (reaction limited) dense structures are formed and gel formation sets in at a higher particle volume fraction and, correspondingly, α is high. Figure 1.21 shows the volume fraction dependence of the G' plateau modulus for a sterically stabilized PS latex dispersion at various concentrations of sodium sulfate (Na_2SO_4) [39]. The stable dispersion shows a strong increase of G' within a narrow concentration range above $\phi = 0.5$, with an exponent $\alpha \approx 30$. At Na_2SO_4 concentrations above the critical flocculation concentration α suddenly decreases and reaches the value of 2.2 at 0.5 M Na_2SO_4, indicating that an open sample-spanning network structure is formed at a particle volume fraction as low as $\phi = 0.35$.

Strongly flocculated dispersions are very sensitive to shear and are characterized by an apparent yield stress. The yield stress σ_y of an aggregated dispersion can be related to the adhesion force F_{adh} between two particles [40]:

$$\sigma_y = \frac{F_{adh}}{a^2} f(\phi) \tag{1.40}$$

The term F_{adh}/a^2 is the stress per particle and for low particle concentration the function $f(\phi)$, referring to the number of particle contacts, can be approximated as the number of binary contacts, that is, $f(\phi) = \phi^2$. The adhesion force is given by the van der Waals attraction, that is, $F_{adh} \approx a$ and thus:

$$\sigma_y \sim \frac{\phi^2}{a} \tag{1.41}$$

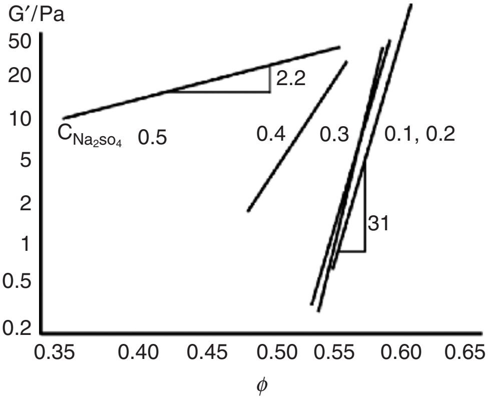

Figure 1.21 Elastic modulus G' versus particle volume fraction ϕ for a sterically stabilized suspension with grafted PEO flocculated by adding Na_2SO_4 [39].

More elaborate models for $f(\phi)$ and the DLVO interaction potential result in the same scaling law and provide good estimates for the absolute value of σ_y and G'. However, various experimental studies [38, 39] have revealed a different scaling for the yield stress of strongly flocculated particulate gels with particle size and volume fraction:

$$\sigma_y \sim \frac{\phi^3}{a^2} \tag{1.42}$$

Capillary Forces in Suspension Rheology Recently, Koos and Willenbacher [41] reported that the addition of small amounts of a secondary fluid, immiscible with the continuous phase of the suspension, can dramatically change the rheological properties of suspensions. Capillary forces between particles lead to the formation of a sample-spanning network structure resulting in a transition from predominantly viscous to gel-like behavior. This phenomenon is observed for various different fluid/particle systems, independent of whether the primary liquid or the secondary immiscible liquid preferentially wet the solid particles. When the secondary fluid creates isolated capillary bridges between particles the observed gel-like state is termed the *"pendular" state*, analogous to the pendular state in wet granular media (see Chapter 2, in Volume 1 [28]). Even if the second, immiscible fluid does not preferentially wet the solid particles it can still attach to the particles and cause agglomeration due to the negative curvature of the solid/liquid interface. This state is analogous to the capillary state in wet granular media close to the saturation limit. Figure 1.22 shows two examples demonstrating the effect of the fraction of

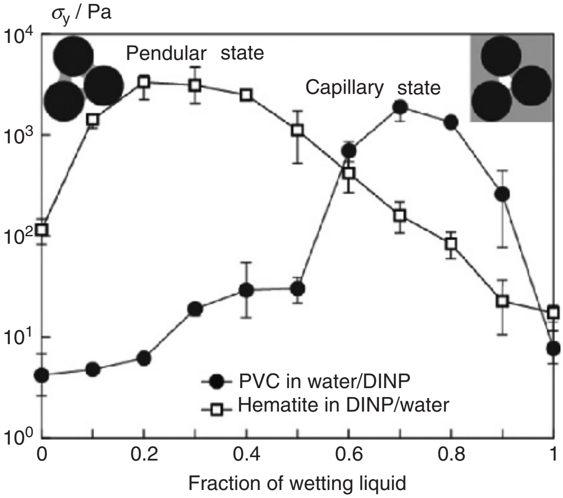

Figure 1.22 Yield stress versus fraction of wetting liquid S. For the aqueous PVC dispersion with addition of DINP the yield stress shows a maximum in the capillary state. On adding water to the suspension of hematite particles in DINP the yield stress shows a maximum in the pendular state.

wetting liquid on the yield stress for both the pendular and the capillary state. The increase in yield stress is greatest in the capillary state for the aqueous poly(vinyl chloride) (PVC) dispersion with diisononyl phthalate (DINP) as a secondary fluid. In contrast, the maximum in the yield stress for the dispersion of hematite particles in DINP is in the pendular state where water is the secondary fluid.

SAOS measurements of suspension in the capillary state clearly demonstrate the transition between the weakly elastic, predominantly viscous to highly elastic, gel-like behavior with increasing amount of secondary fluid. Figure 1.23 shows the frequency dependence of the complex shear modulus G^* for hydrophobically modified calcium carbonate ($CaCO_3$) particles suspended in a silicone oil with different amounts of added water as a secondary fluid. Without the secondary fluid the magnitude of the complex shear modulus $|G^*|$ increases with increasing frequency, whereas on addition of only 0.2% wt. water the complex shear modulus G^* becomes frequency independent. This transition in the rheological properties of a suspension upon adding small amount of a secondary fluid is directly evident from the images shown in Figure 1.24. Note that this phenomenon has been observed at a particle volume fraction as low as about 10%.

This phenomenon has important potential technical applications. The formation of a strong sample-spanning network prevents sedimentation. Furthermore, it changes the rheological properties of the system, which is a reversible process and may be tuned by temperature or addition of surfactant. Another field of application is to use such suspensions as precursors for porous materials. The strong capillary forces prevent the collapse of the network structure upon removal of the liquid phase. A solid PVC foam has been already produced under laboratory conditions, using PVC particles ($\phi = 0.2$) dispersed in water, with DINP as a secondary fluid [41].

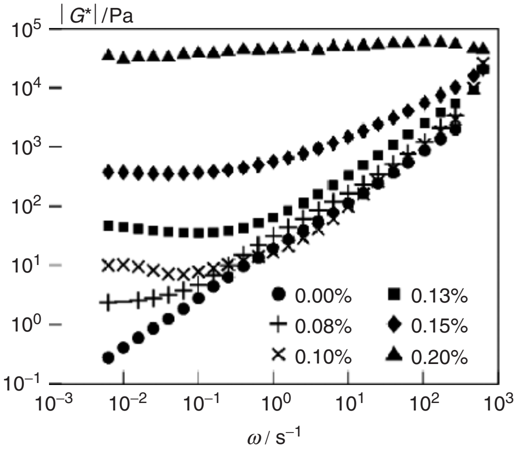

Figure 1.23 Magnitude of complex shear modulus $|G^*|$ versus frequency ω for hydrophobically modified $CaCO_3$ particles ($a = 800$ nm, $\phi = 0.173$) dispersed in a silicone oil, with the addition of various amounts of water.

Fluidization of Highly Concentrated Dispersions Highly concentrated dispersions with a particle volume fraction above the colloidal glass transition ϕ_g behave as gel-like materials with finite plateau modulus G_0. A classical method to keep highly concentrated dispersions fluid and to minimize their viscosity is to shift the maximum packing fraction by mixing of particles of different size (Section 1.4.3). However, in this section we will consider an alternative concept of fluidizing dense colloidal dispersions, based on the so-called re-entry glass transition in colloidal dispersions [42–45].

Weak attractive interactions, for example, introduced by the depletion effect of non-adsorbing polymers dissolved in the continuous phase, can shift the colloidal glass transition ϕ_g to significantly higher values (up to $\phi \approx 0.7$), which can be used to make freely flowing but highly concentrated dispersions. Figure 1.25 shows the viscosity reduction upon addition of a non-adsorbing polymer to an aqueous dispersion of a hard-sphere like polystyrene–(butyl acrylate), P(S-BA), dispersion at a particle volume fraction above the colloidal glass transition [46]. It can be seen

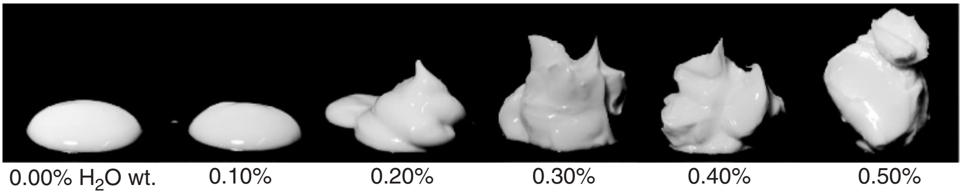

Figure 1.24 Transition from weakly elastic, predominantly viscous to highly elastic, gel-like behavior with increasing amount of water added to a suspension of hydrophobically modified $CaCO_3$ ($a = 800$ nm, $\phi = 0.11$) in DINP.

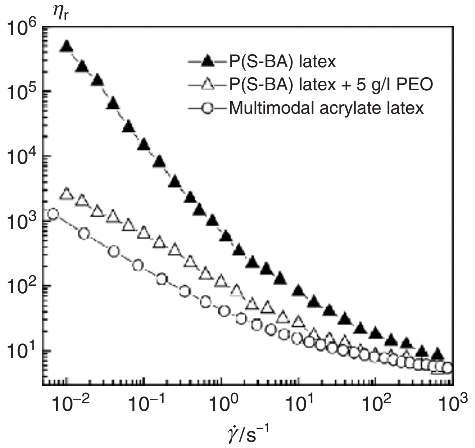

Figure 1.25 Relative viscosity as a function of shear rate for an aqueous polystyrene–(butyl acrylate) P(S-BA) dispersion at $\phi = 0.64$ with and without added PEO ($M_w = 20\ 000\ \mathrm{g\,l^{-1}}$) in comparison with a commercial polymer dispersion (acrylate latex) with a broad multimodal size distribution [46].

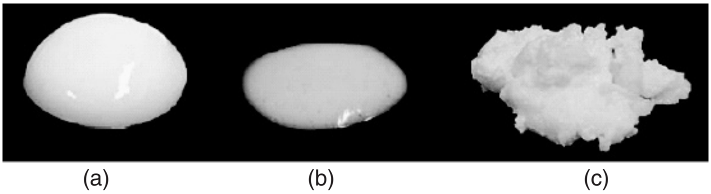

Figure 1.26 Changes in the texture of an aqueous P(S-BA) latex (a) at $\phi = 0.64$ upon addition of different concentrations of PEO ($M_w = 4000\,\mathrm{g\ mol^{-1}}$): (b) 5 and (c) $10\,\mathrm{g\,l^{-1}}$.

that the low-shear viscosity decreases by two orders of magnitude upon addition of non-adsorbing polymer and the effect is comparable to that resulting from broad multimodal particle size distribution. The fluidization of an aqueous latex dispersion due to added non-adsorbing polymer is also evident in Figure 1.26, which shows images of the suspension with different polymer concentration placed on a glass plate. On adding different amounts of PEO to the aqueous P(S-BA) dispersion the texture of the sample changes from gel-like, due to the particle caging at this concentration (repulsive glass), to fluid like and again to gel-like but now due to particle bonding (attractive glass).

1.4.3
Effect of Particle Size Distribution

Numerous experimental studies have been performed using bimodal and multimodal model systems and various phenomenological models have been developed to describe the effect of particle size distribution on viscosity. Typically, a significant viscosity reduction due to mixing particles with different size is observed at particle volume fractions $\phi > 0.5$ and the effect increases with increasing ϕ. For bimodal systems the viscosity at a given particle loading goes through a pronounced minimum at a relative fraction of small particles $\xi_s \approx 0.3$. This viscosity reduction phenomenon is observed for dispersions of non-Brownian as well as Brownian hard spheres. Typical examples are presented in Figure 1.27a,b. Viscosity reduction has been observed at particle size ratios as low as $\chi = 1.7$ and for hard sphere suspensions the effect increases with increasing $\chi = a_{\mathrm{large}}/a_{\mathrm{small}}$. This is no longer true if repulsive colloidal interactions become relevant. At a fixed size of the large particles an increasing χ value corresponds to a decreasing size of small particles a_{small} and if the range of the repulsive interactions is constant this corresponds to an increasing ϕ_{eff}. As a consequence the viscosity goes through a minimum and then increases again if the size ratio χ is increased at a constant total particle concentration and a fixed fraction of small particles. This is shown schematically in Figure 1.28. Willenbacher and coworkers [47, 48] have investigated this phenomenon intensively using a large number of polymer dispersions with different particle size ratio and different range of repulsive interaction. They could show that for typical commercial dispersions with short-range repulsive interactions the viscosity reduction effect is most pronounced at a size ratio $\chi = 4{-}5$. Furthermore,

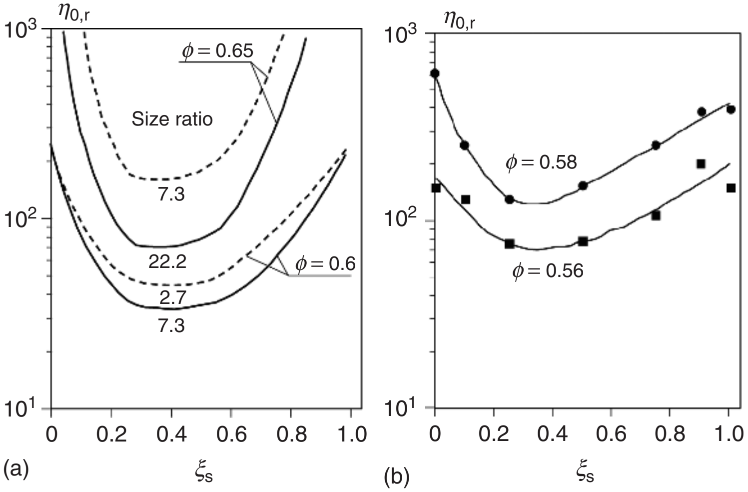

Figure 1.27 Relative zero-shear viscosity $\eta_{0,r}$ versus small particle volume fraction ξ_s: (a) for a suspension of non-Brownian hard spheres at different size ratios (b) For a suspension of Brownian particles with size ratio $\chi = 1.7$ at different particle concentration ϕ (0.58 and 0.56). Redrawn from Rodriguez *et al.* [50].

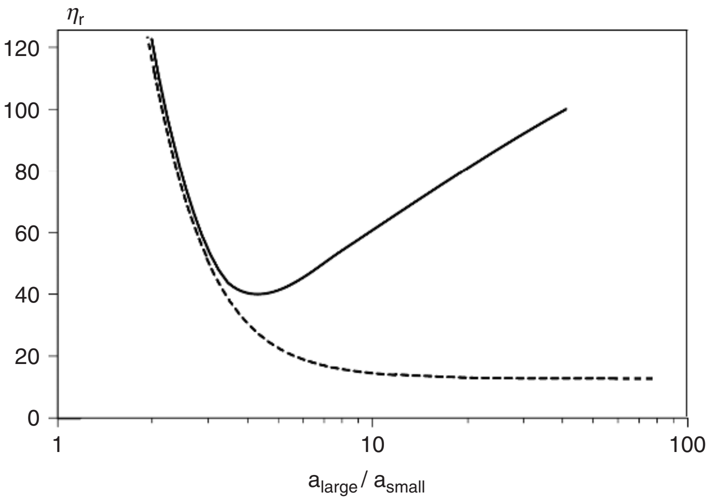

Figure 1.28 Schematic drawing of relative viscosity as a function of particle size ratio calculated according to Equation 1.43 for large particle radius $a_{large} = 400$ nm, total particle concentration $\phi = 0.6$, and small particle volume fraction $\xi_s = 0.25$. The dashed line shows the results for $\varepsilon = 2$, that is, hard sphere dispersions, and the solid line represents the results for ε as a function of average particle size. Adapted from Dames *et al.* [47].

they proposed a generalized Quemada model:

$$\eta = \tilde{\eta}\left(1 - \frac{\phi}{\phi_{\max}}\right)^{-\varepsilon} \tag{1.43}$$

with a shear rate dependent pre-factor $\tilde{\eta}$ and they could show that $\phi_{\max}$ can be calculated solely from the particle size distribution according to a phenomenological model derived from a large set of data for non-colloidal hard sphere packing [51], and the colloidal interactions are parameterized by the exponent $\varepsilon \geq 2$. The exponent ε is equal to 2 in the hard sphere limit and increases with decreasing mean particle size. This is attributed to the fact that colloidal interactions among particles become more important as the mean particle separation diminishes and viscosity diverges at lower volume fractions than expected for hard spheres.

The phenomenon of viscosity reduction due to bi- or multimodal particle size distribution is often attributed to an optimized packing that fits small particles into the interstitial volume between the large particles. Along these lines Farris [52] has developed a model for bimodal dispersions with size ratio $\chi > 10$, treating the small particles together with the solvent as a homogeneous fluid with an effective viscosity and assuming that small and large particles do not interact. This model predicts a viscosity minimum at a small particle fraction $\xi_s = 0.27$, which is in good agreement with many experimental observations. But, on the other hand, a minimum value of $\chi_c = 6.46$ [53] is required to fit a small particle into the interstitial volume within a tetrahedron of large particles and for $\chi = \chi_c$ this packing concept corresponds to a fraction of small particles $\xi_s < 0.01$, which is by far not sufficient to induce a viscosity reduction. However, a small particle volume fraction of $\xi_s \approx 0.3$, which is needed to induce a significant viscosity reduction, corresponds to a number ratio $N_{\text{small}}/N_{\text{large}} \approx 100$ at a size ratio around χ_c. These considerations demonstrate that simple packing considerations are not sufficient to explain the observed phenomena. Accordingly, the formation of ordered superlattice structures or phase separation effects have also been discussed, but a satisfying theory explaining the effect of particle size distribution on viscosity is still lacking.

1.4.4
Shear Thickening

Shear thickening describes the phenomenon of increasing viscosity with increasing shear rate or shear stress. This phenomenon has been observed for a wide variety of colloidal and non-colloidal particle suspensions. Shear thickening becomes important at high shear rates and occurs beyond a critical volume fraction (Figure 1.29a). The thickening effect increases with particle loading and depends on particle size, particle size distribution, and interactions among particles [54].

Early rheological and light scattering results [56, 57] suggested that the shear thickening phenomenon is due to a shear induced order–disorder transition and the shear thinning observed at intermediate shear rates is attributed to the formation of a layered structure. Repulsive interactions are assumed to stabilize this layered structure. At sufficiently high shear rates spatial fluctuations of particle

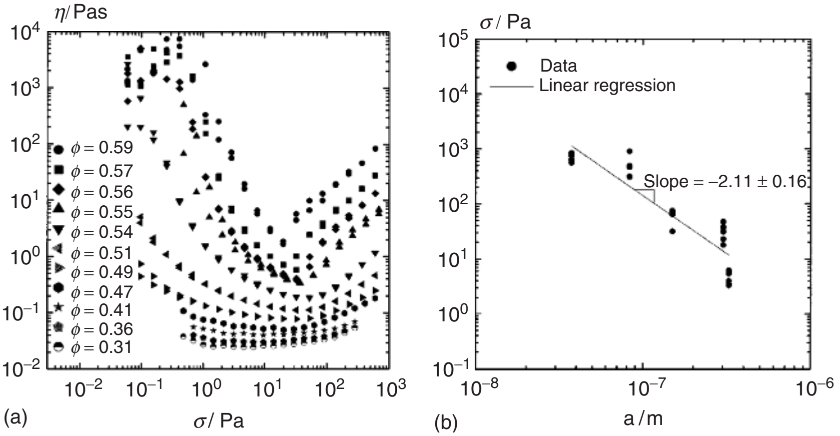

Figure 1.29 Shear thickening of charge stabilized silica dispersions with various particle radii (75, 167, 300, 600, and 1000 nm) and particle volume fraction ranging between 0.31 and 0.59 [55]. (a) Viscosity versus shear stress; (b) critical shear stress σ_c versus particle radius a. The line fits the power law dependence $\sigma_c \approx a^{-2}$. Adapted from Maranzano and Wagner [55].

position destabilize the ordered flow, which results in a strong increase in viscosity. The onset of shear thickening is related to a critical shear rate, above which the hydrodynamic lubrication forces exceed the repulsive colloidal forces [58]. However, comprehensive rheo-optical and small-angle neutron scattering (SANS) experiments [59–62] have revealed that the shear thickening phenomenon may or may not be accompanied by an order–disorder transition but this transition is not a necessary condition. Instead, these investigations clearly revealed that shear thickening is due to the formation of so-called hydroclusters, which form under the action of hydrodynamic forces pushing particles together and instantaneously disintegrate upon cessation of flow. The formation of clusters shows up in turbidity and flow birefringence and has also been confirmed by stress jump experiments [63] as well as Stokesian dynamics simulations of hard sphere dispersion flow [64–66]. Furthermore, Chow and Zukoski [67] investigated the shear thickening behavior of electrostatically stabilized particles in very thin rheometer gaps and found that the critical shear rate for shear thickening increases with increasing the gap size, indicating formation of gap-spanning clusters. The increase in viscosity is attributed to the anisotropic shape of the clusters and the enhanced effective particle volume fraction due to trapped solvent. The hydroclusters can collide with each other and thus ‘‘jam’’ the flow, leading to discontinuous shear thickening at a critical shear stress. If the particle volume fraction is not high enough, hydrocluster formation does not lead to jamming and the shear thickening effect is less pronounced. The formation of hydroclusters is controlled by the balance of hydrodynamic force needed to push particles together and the repulsive thermodynamic forces. Accordingly, a critical stress σ_c for the onset of shear thickening is predicted that scales as $\sigma_c \approx a^{-2}$ for electrostatically stabilized systems, which is consistent with experimental results [55, 58, 61] (Figure 1.29b). This scaling has also been observed for sterically stabilized dispersions [68]. Note that σ_c is almost independent of particle volume fraction ϕ, while the corresponding critical shear rate $\dot{\gamma}_c = \sigma_c/\eta(\phi)$ decreases with increasing ϕ.

Shear thickening can be suppressed or shifted to higher critical stresses by a broad particle size distribution [54]. It has been shown that for bimodal mixtures with size ratio $\chi \approx 3$ the critical shear stress σ_c increases with increasing fraction of small particles ξ_s [55, 61]. Particle shape also has a strong influence on the shear thickening behavior. Beazley [69] demonstrated that anisotropic clay suspensions exhibit shear thickening behavior at lower volume fractions and the effect increases with increasing aspect ratio. Bergstrom [70] investigated aqueous suspensions of rod-shaped silicon carbide whiskers with aspect ratio $r_p \approx 10$ and reported shear thickening behavior at volume fraction as low as 17%. More recently, Egres and Wagner [71] investigated systematically the effect of particle anisotropy on shear thickening using a poly(ethylene glycol) based suspensions of acicular precipitated calcium carbonate (PCC) particles with aspect ratio varying between 2 and 7. Two important results have been pointed out: the critical volume fraction for the onset of shear thickening decreases with increasing aspect ratio but the critical shear stress σ_c is independent of the aspect ratio and follows the scaling laws proposed for hard sphere dispersions with a size corresponding to the minor axis dimension.

1.5
Rheology of Emulsions

The rheology of emulsions exhibits many qualitative analogs to the rheology of solid spherical particle dispersions. Differences arise from the deformability of liquid drops, which is especially relevant at high shear rates and/or high volume fraction of the disperse phase. However, even at low shear rates and low droplet concentrations the relative viscosity of emulsions differs from that of solid sphere dispersions. This is due to circulation of the flow inside the droplets, which leads to deformation of the external streamlines around the fluid spheres such that the flow is less disturbed and viscous dissipation is lower [72]. The degree of this effect depends on the viscosity ratio M:

$$M = \frac{\eta_d}{\eta_s} \tag{1.44}$$

where η_d is the viscosity of the droplet liquid. For high droplet viscosity the viscosity ratio M approaches infinity and the distortion of the stream lines approaches that of rigid spheres. This effect is measurable even in very dilute emulsions and is captured by the Taylor equation [73]:

$$\eta = \eta_s \left[1 + \left(\frac{1 + 2.5M}{1 + M}\right)\phi\right] \tag{1.45}$$

which reduces to the Einstein equation (Equation 1.24) for $M \to \infty$. Taylor's hydrodynamic theory assumes no deformation of droplets, which is satisfied at low enough shear rates. In typical oil-in-water (O/W) emulsions the interfacial tension Γ is high enough to counteract the effect of hydrodynamic forces and leads to fast shape relaxation. The droplet relaxation time τ_{d} is given by:

$$\tau_{\mathrm{d}} = \frac{a\eta_{\mathrm{s}}}{\Gamma} \tag{1.46}$$

and droplet deformation is not relevant for emulsion rheology as long as $\dot{\gamma} < \tau_{\mathrm{d}}^{-1}$. The balance between surface tension and shear forces is often expressed by the dimensionless capillary number (Ca):

$$\mathrm{Ca} = \frac{a\eta_{\mathrm{s}}\dot{\gamma}}{\Gamma} \tag{1.47}$$

Droplet deformation and rupture occur at Ca > 1. A closer look at the phenomenon reveals that the critical Ca at which droplet rupture occurs depends strongly on the viscosity ratio M and can vary by orders of magnitude [74, 75]. Flow kinematics also plays a role and, generally, droplet rupture is easier in elongational than in shear flow.

Experimental results on model emulsions of different viscosity ratios M, reported by Nawab and Mason [76] demonstrated excellent agreement with Taylor's hydrodynamic theory (Figure 1.30). Nawab and Mason pointed out that in some cases adsorbed surfactant layers can reduce the internal circulations and thereby cause an increase of intrinsic viscosity to the rigid sphere limit.

With increasing concentration above the Einstein limit, hydrodynamic interactions become significant and Taylor's equation cannot describe the volume fraction–viscosity dependence. Pal [77] has proposed a phenomenological viscosity equation for concentrated emulsions that takes into account the effect of viscosity ratio M and reduces to the generalized Krieger–Dougherty equation (Equation 1.26)

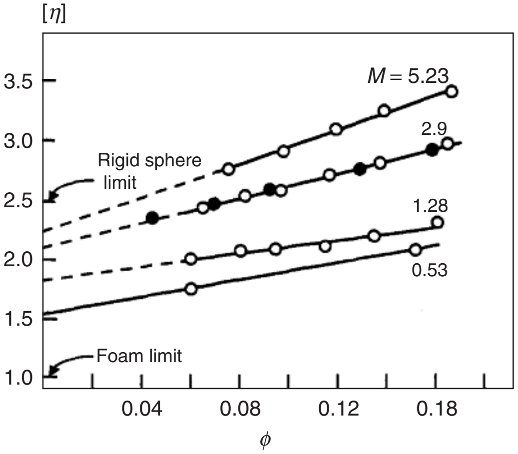

Figure 1.30 Intrinsic viscosity $[\eta]$ versus droplet volume fraction ϕ for monodisperse emulsions of butyl benzoate oil droplets in different water solutions in order to vary the viscosity ratio M [76]. Taken from Macosko [8]. Copyright © 1994 John Wiley & Sons.

when $M \to \infty$:

$$\eta_r \left[\frac{2\eta_r + 5M}{2 + 5M}\right]^{3/2} = \left[1 - \frac{\phi}{\phi_{\max}}\right]^{-2.5\phi_{\max}} \tag{1.48}$$

This equation as based on a large set of experimental data for emulsions covering a broad range of droplet volume fractions ϕ and viscosity ratios M.

The effect of dispersed phase volume fraction on rheology of typical technical emulsions is less severe in comparison to colloidal dispersions. Since droplet size is usually in the micron range technically relevant shear rates correspond to very high Pe numbers and the measured viscosity data correspond to the upper Newtonian plateau regime. Viscosity is further reduced at high droplet volume fractions due to the usually broad droplet size distributions. As a consequence such emulsions behave as Newtonian fluids up to volume fractions close to dense packing ($\phi \approx 0.6$) [78]. Emulsions with an average droplet radius in the range of several 100 nm exhibit a flow behavior resembling very much that of colloidal hard sphere suspensions. Note that increasing the volume fraction of the dispersed phase does not necessarily result in a monotonic increase in viscosity. At a critical droplet volume fraction, phase inversion may occur that is accompanied by a drastic drop in viscosity. However, emulsions are usually stabilized by surfactants adsorbed onto the droplet surface that prevent the coalescence of droplets at contact.

Repulsive and attractive colloidal interactions as well as droplet deformation and rupture during flow can cause a deviation from the hard sphere behavior of emulsions. The effect of repulsive droplet interactions due to surface charge or adsorbed polymer can be captured by hard sphere mapping ($\phi \to \phi_{\text{eff}}$) similar to that for suspensions of repulsive solid particles. Attractive droplet interactions lead to flocculation and gelation analogously to attractive particle suspensions. Emulsion rheology can be tuned over a wide range by adding thickeners to the continuous phase or by excess surfactant providing self-assembling gel-like structure to the continuous phase, which is particularly relevant for stabilization against creaming.

Emulsions can exhibit distinct viscoelastic properties even if both constituents are Newtonian fluids due to the contribution of the interfacial tension, which opposes droplet deformation. This is particularly important for polymer blends, where the viscosity of both components is high and deformed interfaces relax slowly. Various models have been established to describe the complex shear modulus G^* of emulsions. When both phases are Newtonian the Oldroyd model [79, 80] suits:

$$G^* = \mathrm{i}\omega\eta_s \left(\frac{1 + \frac{3}{2}\phi\frac{E}{D}}{1 - \phi\frac{E}{D}}\right) \tag{1.49}$$

with:

$$E = 2\mathrm{i}\omega(\eta_d - \eta_s)(19\eta_d + 16\eta_s) + \frac{8\Gamma}{a}(5\eta_d + 2\eta_s)$$

$$D = \mathrm{i}\omega(2\eta_d + 3\eta_s)(19\eta_d + 16\eta_s) + \frac{40\Gamma}{a}(\eta_d + \eta_s) \tag{1.50}$$

For emulsions with viscosity ratio $M \to \infty$, droplets behave like solid particles and the droplet relaxation time is so short that the ratio E/D reduces to:

$$\frac{E}{D} = \frac{0.4 + M}{1 + M} \tag{1.51}$$

In the dilute limit with $\phi \to 0$, Equation 1.49 simplifies to:

$$G^* = \mathrm{i}\omega\eta_\mathrm{s}\left(1 + \frac{5}{2}\phi\frac{E}{D}\right) \tag{1.52}$$

For emulsions where both continuous and dispersed phase are viscoelastic with frequency dependent complex moduli G_s^* and G_d^*, respectively, the Palierne [81] model provides a good description for the complex modulus G^* of the emulsion:

$$G^* = G_\mathrm{s}^*\left(\frac{1 + \frac{3}{2}\phi\frac{E}{D}}{1 - \phi\frac{E}{D}}\right) \tag{1.53}$$

with:

$$\begin{aligned} E &= 2(G_\mathrm{d}^* - G_\mathrm{s}^*)(19G_\mathrm{d}^* + 16G_\mathrm{s}^*) + \frac{8\Gamma}{a}(5G_\mathrm{d}^* + 2G_\mathrm{s}^*) \\ D &= (2G_\mathrm{d}^* + 3G_\mathrm{s}^*)(19G_\mathrm{d}^* + 16G_\mathrm{s}^*) + \frac{40\Gamma}{a}(G_\mathrm{d}^* + G_\mathrm{s}^*) \end{aligned} \tag{1.54}$$

Kitade *et al.* [82] investigated the viscoelastic properties of polymer blends consisting of polydimethylsiloxane (PDMS) and polyisoprene and demonstrated that the

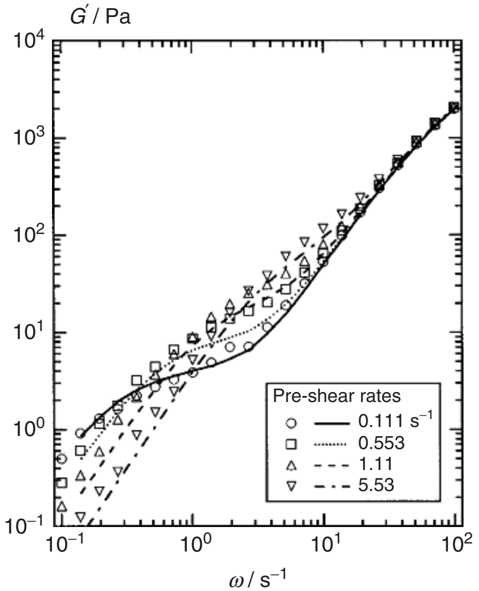

Figure 1.31 Comparison of the Palierne model (lines) with measured $G'(\omega)$ dependence for a blend of 11% polyisoprene ($\eta_0 = 60.9$ Pa s) in PDMS ($\eta_0 = 73.7$ Pa s) with $\Gamma = 3.2$ mN m^{-1}, pre-sheared at four different shear rates [82].

experimentally determined frequency dependence of G' is in agreement with the Palierne model (Figure 1.31). The contribution of the interfacial term results in a pronounced shoulder in the $G'(\omega)$ curve in the low frequency range. Figure 1.31 shows that with increasing pre-shear rate, which corresponds to a decrease of the average droplet size [82], the "shoulder" in the $G'(\omega)$ dependence shifts to higher frequencies. This is due to an increased interfacial area and hence a more pronounced interfacial contribution for smaller droplets. In the high frequency limit the interfacial terms can be ignored and G' is determined only by the viscoelasticity of the dispersion medium. Then, if $G_\mathrm{d}^*/G_\mathrm{s}^* \approx 1$, the Palierne emulsion model further simplifies to:

$$G^* \approx (1-\phi)G_\mathrm{s}^* + \phi G_\mathrm{d}^* \tag{1.55}$$

Emulsions exhibit unique flow properties that are not observable in suspensions when a critical volume fraction ϕ_c is exceeded. For colloidal systems ϕ_c may be associated with the glass transition and for non-Brownian systems with the volume fraction of close packing. At volume fractions $\phi > \phi_\mathrm{c}$ dispersions of solid particles can no longer flow. In contrast, emulsions still flow even at $\phi > \phi_\mathrm{c}$ since droplets start to deform and take a polyhedral shape. Such emulsions exhibit an apparent yield stress, strong shear thinning, and pronounced elasticity. In the linear viscoelastic regime the storage modulus G' is much larger than G'' and essentially independent of frequency; this G' value is known as the *plateau modulus* G_0. Steady shear flow curves are usually well described by the Herschel–Bulkley model:

$$\sigma = \sigma_\mathrm{y} + k\dot{\gamma} \tag{1.56}$$

where k is the consistency parameter and n the power law index. The apparent yield stress, the degree of shear thinning (here expressed in terms of n), and the plateau modulus increase with increasing volume fraction of internal phases and decreasing droplet size. A thermodynamic model developed by Princen [83] related the droplet compression to the osmotic pressure in the system, which increases with increasing droplet volume fraction ϕ. When the osmotic pressure exceeds the Laplace pressure Γ/a droplets start to deform and pack more tightly with increasing ϕ. The elasticity of the system then arises from the surface tension acting to resist the deformation. The plateau modulus G_0 gradually develops when ϕ_c is approached and then increases linearly with effective volume fraction [84]:

$$G_0 = \frac{3\Gamma}{2a}(\phi_\mathrm{eff} - \phi_\mathrm{c}) \tag{1.57}$$

where ϕ_eff accounts for the excluded volume due to repulsive forces. G_0 is also proportional to the Laplace pressure Γ/a and when ϕ_eff approaches unity the plateau modulus approaches the limiting value $G_0 \approx \Gamma/2a$.

Densely packed emulsions with $\phi > \phi_\mathrm{c}$ are characterized by an apparent yield stress σ_y at which the rest structure breaks down. In oscillatory shear measurements, yielding occurs at a critical deformation amplitude, called the *yield strain* $\gamma_\mathrm{y} = \sigma_\mathrm{y}/G_0$. For highly concentrated emulsions this yield strain increases linearly with increasing droplet volume fraction [85]:

$$\gamma_\mathrm{y} \sim (\phi_\mathrm{eff} - \phi_\mathrm{c}) \tag{1.58}$$

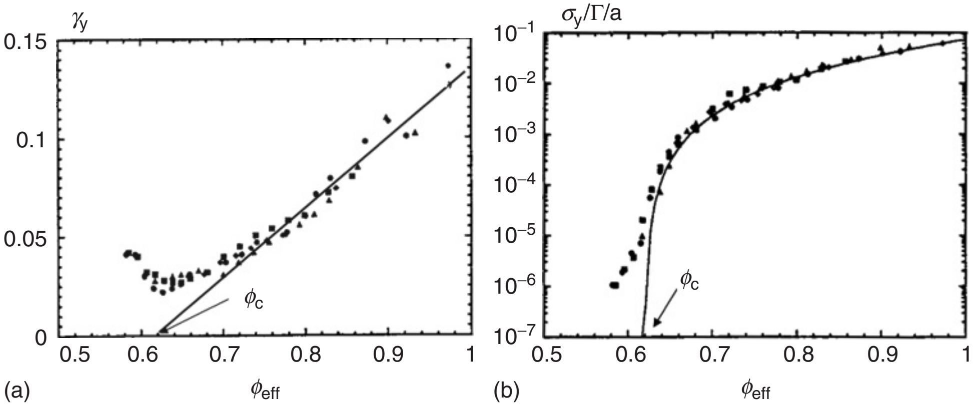

Figure 1.32 (a) Yield strain γ_y versus effective volume fraction ϕ_{eff}; solid line corresponds to Equation 1.58; (b) apparent yield stress σ_y scaled by the Laplace pressure (Γ/a) versus ϕ_{eff} for monodispersed emulsions with droplet size (nm): $a = 250$ (circles), 370 (triangles), 530 (squares), and 740 (diamonds); solid line corresponds to Equation 1.57 [85].

Figure 1.32a demonstrates this linear dependence for monodispersed emulsions having different droplet size. Obviously, the volume fraction dependence of γ_y is independent of droplet size and γ_y reaches its minimum at ϕ_c. The yield stress σ_y can be approximately expressed as $\sigma_y = G_0\gamma_y$ and together with Equation 1.57 this yields the following relationship:

$$\sigma_\gamma = \frac{3}{2}\frac{\Gamma}{a}(\phi_{eff} - \phi_c)^2 \tag{1.59}$$

which nicely fits the experimental data in Figure 1.32b. For $\phi_{eff} \approx 1$ Equation 1.59 roughly reduces to:

$$\sigma_y(\phi_{eff} = 1) \approx 0.1\frac{\Gamma}{a} \tag{1.60}$$

These experimental findings are also captured by the Princen–Kiss model [86]:

$$\sigma_y = \frac{\Gamma}{a}\phi^{\frac{1}{3}}Y(\phi) \tag{1.61}$$

This model is based on the affine deformation of a hexagonal structure and $Y(\phi)$ can be expressed in analytical form for two-dimensional systems; however, for three-dimensional emulsions $Y(\phi)$ is an empirical function:

$$Y(\phi) = -0.080 - 0.114 lg(1-\phi) \tag{1.62}$$

Also distinct in a mathematical sense, the absolute numerical values of the terms $\phi^{1/3}(\phi)$ and $(\phi_{eff} - \phi_c)$ are not very different and ϕ_{eff} does not differ much from ϕ if the layer immobilized by the surfactant is small compared to the droplet size, as for many technically relevant emulsions. Equations 1.59 and 1.61 include the linear relationship between σ_y and the Laplace pressure Γ/a; if the particle size a is known, measuring σ_y or preferentially G_0, since it is accessible with high accuracy

(Equation 1.57), is a valuable tool for determining the interfacial tension Γ, which is otherwise often hard to access.

Highly concentrated emulsions often do not exhibit uniform deformation even in simple shear flow, instead they show shear banding, which can be very irregular in the sense that the plane of deformation changes its position or that the width of the deformed region changes with time [87–90].

References

1. Tadros, T.F. (2010) *Rheology of Dispersions – Principles and Application*, Wiley-VCH Verlag GmbH, Weinheim.
2. James, D.F. and Walters, K. (1993) A critical appraisal of available methods of extensional properties of mobile systems in techniques, in *Rheological Measurements* (ed. A.A. Collyer), Elsevier, London.
3. Willenbacher, N. and Hingmann, R. (1994) Shear and elongational flow properties of fluid S1 from rotational, capillary, and opposed jet rheometry. *J. Non-Newtonian Fluid Mech.*, **52**, 163–176.
4. McKinley, G.H. and Sridhar, T. (2002) Filament-stretching rheometry of complex fluids. *Annu. Rev. Fluid Mech.*, **34**, 375–415.
5. McKinley, G.H. (2005) Visco-elasto-capillary thinning and break-up of complex fluids. *Rheol. Rev.*, **3**, 1–48.
6. Niedzwiedz, K., Buggisch, H., and Willenbacher, N. (2010) Extensional rheology of concentrated emulsions as probed by capillary breakup elongational rheometry (CaBER). *Rheol. Acta*, **49**, 1103–1116.
7. Giesekus, H. and Langer, G. (1977) Die bestimmung der wahren fliesskurven nicht-Newtonscher flüssigkeiten und plastischer stoffe mit der methode der repräsentativen viskosität. *Rheol. Acta*, **16**, 1–22.
8. Macosko, C.W. (1994) *Rheology Principles, Measurements, and Applications*, John Wiley & Sons, Inc., New York.
9. Schümmer, P. and Worthoff, R.H. (1978) An elementary method for the evaluation of the flow curve. *Chem. Eng. Sci.*, **33** (6), 759–763.
10. Bagley, E.B. (1957) End corrections in the capillary flow of polyethylene. *J. Appl. Phys.*, **28**, 624–627.
11. Mooney, M. (1931) Explicit formulas for slip and fluidity. *J. Rheol.*, **2**, 210–222.
12. Pusey, P.N. and van Megen, W. (1986) Phase behaviour of concentrated suspensions of nearly hard colloidal spheres. *Nature*, **320**, 340–342.
13. Einstein, A. (1906) Eine neue bestimmung der moleküldimensionen. *Ann. Phys.*, **19**, 289–306.
14. Einstein, A. (1911) Berichtigung zu meiner arbeit: eine neue bestimmung der moleküldimensionen. *Ann. Phys.*, **34**, 591–592.
15. Batchelor, G.K. (1977) The effect of Brownian motion on the bulk stress in a suspension of spherical particles. *J. Fluid Mech.*, **83**, 97–117.
16. Krieger, I.M. and Dougherty, T.J. (1959) A mechanism for non-Newtonian flow in suspensions of rigid spheres. *Trans. Soc. Rheol.*, **3**, 137–152.
17. Quemada, D. (1977) Rheology of concentrated disperse systems and minimum energy dissipation principle I. Viscosity-concentration relationship. *Rheol. Acta*, **16**, 82–94.
18. Buscall, R., D'Haene, P., and Mewis, J. (1994) Maximum density for flow of dispersions of near monodisperse spherical-particles. *Langnuir*, **10** (5), 1439–1441.
19. van Megen, W., Pusey, P.N., and Bartlett, P. (1990) Phase behavior of dispersions of hard spherical particles. *Phase Transitions*, **21** (2–4), 207–227.
20. van Megen, W. and Underwood, S.M. (1994) Glass transition in colloidal hard spheres: measurement and mode-coupling-theory analysis of the coherent

intermediate scattering function. *Phys. Rev. E*, **49**, 4206–4220.

21. Meeker, S.P., Poon, W.C.K., and Pusey, P.N. (1997) Concentration dependence of the low-shear viscosity of suspensions of hard-sphere colloids. *Phys. Rev. E*, **55**, 5718–5722.
22. Phan, S.-E., Russel, W.B., Cheng, Z., and Zhu, J. (1996) Phase transition, equation of state, and limiting shear viscosities of hard sphere dispersions. *Phys. Rev. E*, **54**, 6633–6645.
23. Choi, G.N. and Krieger, I.M. (1986) Rheological studies on sterically stabilized model dispersions of uniform colloidal spheres 2. Steady-shear viscosity. *J. Colloid Interface Sci.*, **113** (1), 101–113.
24. Krieger, I.M. (1972) Rheology of monodisperse latices. *Adv. Colloid Interface Sci.*, **3**, 111–136.
25. Brenner, H. (1974) Rheology of a dilute suspension of axisymmetric Brownian particles. *Int. J. Multiphase Flow*, **1** (2), 195–341.
26. Giesekus, H. (1983) in *Physical Properties of Foods* (eds R. Jowitt *et al.*), Applied Science Publishers, London, pp. 205–220.
27. Barnes, H.A., Hutton, J.F., and Walters, K. (eds) (1989) *An Introduction to Rheology*, Elsevier Science, Amsterdam.
28. Bröckel, U., Meier, W., and Wagner, G. (eds) (2007) *Product Design and Engineering*: Volume 1, Basics and Technologies, Wiley-VCH Verlag GmbH, Weinheim.
29. Horn, F.M., Richtering, W., Bergenholtz, J., Willenbacher, N., and Wagner, N.J. (2000) Hydrodynamic and colloidal interactions in concentrated charge-stabilized polymer dispersions. *J. Colloid Interface Sci.*, **225**, 166–178.
30. Fritz, G., Schädler, V., Willenbacher, N., and Wagner, N.J. (2002) Electrosteric stabilization of colloidal dispersions. *Langmuir*, **18** (16), 6381–6390.
31. Wetz, D.A. and Oliveria, M. (1984) Fractal structures formed by kinetic aggregation of aqueous gold colloids. *Phys. Rev. Lett.*, **52** (16), 1433–1436.
32. Weitz, D.A., Huang, J.S., Lin, M.Y., and Sung, J. (1985) Limits of the fractal dimensions for irreversible kinetic aggregation of gold colloids. *Phys. Rev. Lett.*, **54** (13), 1416–1419.
33. Sonntag, R.C. and Russel, W.B. (1986) Structure and breakup of flocs subjected to fluid stresses: I. Shear experiments. *J. Colloid Interface Sci.*, **113** (2), 399–413.
34. Woutersen, A.T.J.M. and de Kruif, C.G. (1991) The rheology of adhesive hard-sphere dispersions. *J. Chem. Phys.*, **94** (8), 5739–5750.
35. Buscall, R., McGowan, J.I., and Morton-Jones, A.J. (1993) The rheology of concentrated dispersions of weakly-attracting colloidal particles with and without wall slip. *J. Rheol.*, **37** (4), 621–641.
36. Buscall, R., Mills, P.D.A., and Yates, G.E. (1986) Viscoelastic properties of strongly flocculated polystyrene latex dispersions. *Colloids Surf.*, **18** (2–4), 341–358.
37. Buscall, R., McGowan, I.J., Mills, P.D.A., Stewart, R.F., Sutton, D., White, L.R., and Yates, G.E. (1987) The rheology of strongly flocculated suspensions. *J. Non-Newtonian Fluid Mech.*, **24** (2), 183–202.
38. Buscall, R., Mills, P.D.A., Goodwin, J.W., and Lawson, D.W. (1988) Scaling behavior of the rheology of aggregate networks formed from colloidal particles. *J. Chem. Soc., Faraday Trans.*, **84** (12), 4249–4260.
39. Tadros, T.F. (1996) Correlation of viscoelastic properties of stable and flocculated suspensions with their interparticle interactions. *Adv. Colloid Interface Sci.*, **68**, 97–200.
40. Larson, R.G. (1999) *The Structure and Rheology of Complex Fluids*, Oxford University Press, New York.
41. Koos, E. and Willenbacher, N. (2011) Capillary forces in suspension rheology. *Science*, **331** (6019), 897–900.
42. Pham, K.N., Puertas, A.N., Bergenholtz, J., Egelhaaf, S.U., Moussaidl, A., Pusey, P.N., Schofield, A.B., Cates, M.E., Fuchs, M., and Poon, W.C.K. (2002) Multiple glassy state in a simple model system. *Science*, **296** (5565), 104–106.
43. Pham, K.N., Egelhaaf, S.U., Pusey, P.N., and Poon, W.C.K. (2004)

Glasses in hard spheres with short-range attraction. *Phys. Rev. E*, **69** (1), 011503.1–011503.13.

44. Eckert, T. and Bartsch, E. (2002) Re-entrant glass transition in a colloid-polymer mixture with depletion attractions. *Phys. Rev. Lett.*, **89** (12), 125701–125704.

45. Eckert, T. and Bartsch, E. (2004) Glass transition dynamics of hard sphere like microgel colloids with short-ranged attractions. *J. Phys. Condens. Matter*, **16**, S4937–S4950.

46. Willenbacher, N., Vesaratchanon, J.S., Thorwarth, O., and Bartsch, E. (2011) An alternative route to highly concentrated, freely flowing colloidal dispersions. *Soft Matter*, **7**, 5777–5788.

47. Dames, B., Morrison, B.R., and Willenbacher, N. (2001) An empirical model predicting the viscosity of highly concentrated, bimodal dispersions with colloidal interactions. *Rheol. Acta*, **40** (5), 434–440.

48. Willenbacher, N., Börger, L., Urban, D., and Varela de la Rosa, L. (2003) Tailoring PSA-dispersion rheology for high-speed coating. *Adhesives Sealants Ind.*, **10** (9), 25–35.

49. Chong, J.S., Christiansen, E.B., and Baer, A.D. (1971) Rheology of concentrated suspensions. *J. Appl. Polym. Sci.*, **15** (8), 2007–2021.

50. Rodriguez, B.E., Kaler, E.W., and Wolfe, M.S. (1992) Binary mixtures of monodisperse latex dispersions 2. Viscosity. *Langmuir*, **8** (10), 2382–2389.

51. Sudduth, R.D. (1993) A generalized model to predict the viscosity of solutions with suspended particles I. *J. Appl. Polym. Sci.*, **48** (1), 25–36.

52. Farris, R.J. (1968) Prediction of the viscosity of multimodal suspensions from unimodal viscosity data. *Trans. Soc. Rheol.*, **12** (2), 281–301.

53. McGeary, R.K. (1961) Mechanical packing of spherical particles. *J. Am. Ceram. Soc.*, **44** (10), 513–522.

54. Barnes, H.A. (1989) Shear-thickening (''Dilatancy'') in suspensions of nonagregating solid particles dispersed in Newtonian liquids. *J. Rheol.*, **33** (2), 329–366.

55. Maranzano, B.J. and Wagner, N.J. (2001) The effect of particle size on reversible shear thickening of concentrated colloidal dispersions. *J. Chem. Phys.*, **114** (23), 10514–10527.

56. Hoffman, R.L. (1972) Discontinuous and dilatant viscosity behavior in concentrated suspensions I. Observation of a flow instability. *Trans. Soc. Rheol.*, **16** (1), 155–173.

57. Hoffman, R.L. (1974) Discontinuous and dilatant viscosity behavior in concentrated suspensions II. Theory and experimental tests. *J. Chem. Phys.*, **46** (3), 491–506.

58. Boersma, W.H., Laven, J., and Stein, H.N. (1990) Shear thickening (dilatancy) in concentrated suspensions. *AIChE J.*, **36** (3), 321–332.

59. Laun, H.M., Bung, R., and Schmidt, F. (1991) Rheology of extremely shear thickening polymer dispersions (passively viscosity switching fluids). *J. Rheol.*, **35** (6), 999–1034.

60. Laun, H.M., Bung, R., Hess, S., Loose, W., Hahn, K., Hadicke, E., Hingmann, R., Schmidt, F., and Lindner, P. (1992) Rheological and small angle neutron scattering investigation of shear-induced particle structures of concentrated polymer dispersions. *J. Rheol.*, **36** (4), 743–787.

61. Bender, J. and Wagner, N.J. (1996) Reversible shear thickening in monodisperse and bidisperse colloidal dispersions. *J. Rheol.*, **40** (5), 899–916.

62. Bender, J.W. and Wagner, N.J. (1995) Optical measurement of the contributions of colloidal forces to the rheology of concentrated suspension. *J. Colloid Interface Sci.*, **172** (1), 171–184.

63. Kaffashi, B., O'Brien, V.T., Mackay, M.E., and Underwood, S.M. (1997) Elastic-like and viscous-like components of the shear viscosity for nearly hard sphere, Brownian suspensions. *J. Colloid Interface Sci.*, **181** (1), 22–28.

64. Brady, J.F. and Bossis, G. (1988) Stokesian dynamics. *Ann. Rev. Fluid Mech.*, **20**, 111–157.

65. Brady, J.F. and Bossis, G. (1989) The rheology of Brownian suspensions. *J. Chem. Phys.*, **91** (3), 1866–1874.

66. Phung, T.N., Brady, J.F., and Bossis, G. (1996) Stokesian dynamics simulation of Brownian suspensions. *J. Fluid Mech.*, **313**, 181–207.

67. Chow, M.K. and Zukoski, C.F. (1995) Gap size and shear history dependencies in shear thickening of a suspension ordered at rest. *J. Rheol.*, **39** (1), 15–32.

68. Krishnamurthy, L.N. and Wagner, N.J. (2005) Shear thickening in polymer stabilized colloidal dispersions. *J. Rheol.*, **49** (6), 1347–1360.

69. Beazley, K.M. (1980) Industrial aqueous suspensions, in *Rheometry: Industrial Applications* (ed. K. Walters), Research Studies Press, Chichester.

70. Bergstrom, L. (1998) Shear thinning and shear thickening of concentrated ceramic suspensions. *Colloids Surf., A*, **133**, 151–155.

71. Egres, R.G. and Wagner, N.J. (2005) The rheology and microstructure of acicular precipitated calcium carbonate colloidal suspensions through the shear thickening transition. *J. Rheol.*, **49** (3), 719–746.

72. Bartok, W. and Mason, S.G. (1958) Particle motions in sheared suspensions: VII. Internal circulation in fluid droplets (theoretical). *J. Colloid Interface Sci.*, **13** (4), 293–307.

73. Taylor, G.I. (1932) The viscosity of a fluid containing small drops of another fluid. *Proc. R. Soc. London, Ser. A*, **138** (834), 41–48.

74. Grace, H.P. (1982) Dispersion phenomena in high viscosity immiscible fluid systems and application of static mixers as dispersion devices in such systems. *Chem. Eng. Commun.*, **14** (3), 225–277.

75. Zhao, X. (2007) Drop breakup in dilute Newtonian emulsions in simple shear flow: new drop breakup mechanisms. *J. Rheol.*, **51** (3), 367–392.

76. Nawab, M.A. and Mason, S.G. (1985) The viscosity of dilute emulsions. *Trans. Faraday Soc.*, **54**, 1712–1723.

77. Pal, R. (2001) Novel viscosity equations for emulsions of two immiscible liquids. *J. Rheol.*, **45** (2), 509–520.

78. Pal, R. (2000) Shear viscosity behavior of emulsions of two immiscible liquids. *J. Colloid Interface Sci.*, **225** (2), 359–366.

79. Oldroyd, J.G. (1953) The elastic and viscous properties of emulsions and suspensions. *Proc. R. Soc. London, Ser. A*, **218** (1132), 122–132.

80. Oldroyd, J.G. (1955) The effect of interfacial stabilizing films on the elastic and viscous properties of emulsions. *Proc. R. Soc. London, Ser. A*, **232** (1191), 567–577.

81. Palierne, J.F. (1990) Linear rheology of viscoelastic emulsions with interfacial tension. *Rheol. Acta*, **29** (3), 204–214.

82. Kitade, S., Ichikawa, A., Imura, M., Takahashi, Y., and Noda, I. (1997) Rheological properties and domain structures of immiscible polymer blends under steady and oscillatory shear flows. *J. Rheol.*, **41** (5), 1039–1060.

83. Princen, H.M. (1986) Osmotic pressure of foams and highly concentrated emulsions. 1. Theoretical considerations. *Langmuir*, **2** (4), 519–524.

84. Mason, T.G., Lacasse, M.-D., Grest, S.G., Levine, D., Bibette, J., and Weitz, D.A. (1997) Osmotic pressure and viscoelastic shear moduli of concentrated emulsions. *Phys. Rev. E*, **56** (3), 3150–3166.

85. Mason, T.G., Bibette, J., and Weitz, D.A. (1996) Yielding and flow of monodisperse emulsion. *J. Colloid Interface Sci.*, **179** (2), 439–448.

86. Princen, H.M. and Kiss, A.D. (1986) Rheology of foams and highly concentrated emulsions: 3. Static shear modulus. *J Colloid Interface Sci.*, **112** (2), 427–437.

87. Bécu, L., Grondin, P., Colin, A., and Manneville, S. (2004) How does a concentrated emulsion flow? Yielding, local rheology, and wall slip. *Colloids Surf., A*, **263** (1–3), 146–152.

88. Fall, A., Paredes, J., and Bonn, D. (2010) Yielding and shear banding in soft glassy materials. *Phys. Rev. Lett.*, **105** (22), 225502.

89. Callaghan, P.T. (2008) Rheo-NMR and shear banding. *Rheol. Acta*, **47** (3), 243–255.

90. Coussot, P. and Ovarlez, G. (2010) Physical origin of shear-banding in jammed systems. *Eur. Phys. J. E*, **33** (3), 183–188.